

A Climatological Analysis of Ambient Deep-Tropospheric Vertical Wind Shear Impacts upon Tornadoes in Tropical Cyclones

BENJAMIN A. SCHENKEL

*Cooperative Institute for Mesoscale Meteorological Studies, and School of Meteorology,
University of Oklahoma, and NOAA/National Severe Storms Laboratory, Norman, Oklahoma*

ROGER EDWARDS

NOAA/Storm Prediction Center, Norman, Oklahoma

MICHAEL CONIGLIO

NOAA/National Severe Storms Laboratory, Norman, Oklahoma

(Manuscript received 25 October 2019, in final form 24 July 2020)

ABSTRACT

The cyclone-relative location and variability in the number of tornadoes among tropical cyclones (TCs) are not completely understood. A key understudied factor that may improve our understanding is ambient (i.e., synoptic-scale) deep-tropospheric (i.e., 850–200-hPa) vertical wind shear (VWS), which impacts both the symmetry and strength of deep convection in TCs. This study conducts a climatological analysis of VWS impacts upon tornadoes in TCs from 1995 to 2018, using observed TC and tornado data together with radiosondes. TC tornadoes were classified by objectively defined VWS categories, derived from reanalyses, to quantify the sensitivity of tornado frequency, location, and their environments to VWS. The analysis shows that stronger VWS is associated with enhanced rates of tornado production—especially more damaging ones. Tornadoes also become localized to the downshear half of the TC as VWS strengthens, with tornado location in strongly sheared TCs transitioning from the downshear-left quadrant in the TC inner core to the downshear-right quadrant in the TC outer region. Analysis of radiosondes shows that the downshear-right quadrant in strongly sheared TCs is most frequently associated with sufficiently strong near-surface speed shear and veering aloft, and lower-tropospheric thermodynamic instability for tornadoes. These supportive kinematic environments may be due to the constructive superposition of the ambient and TC winds, and the VWS-induced downshear enhancement of the TC circulation among other factors. Together, this work provides a basis for improving forecasts of TC tornado frequency and location.

1. Introduction

Tornadoes often occur in landfalling tropical cyclones (TCs), compounding the damage caused by other hazards [e.g., flooding from Hurricanes Harvey (2017) and Florence (2018); [Blake and Zelinsky 2018](#); [Stewart and Berg 2019](#)]. The fundamental characteristics of tornadoes in landfalling TCs have been well studied. Specifically, ~93% of TC tornadoes have damage rated between enhanced Fujita (EF) or Fujita (F) scale ratings of EF/F0–1, compared to ~90% of non-TC tornadoes

([Edwards 2010, 2012](#)). Supercells, which are frequently classified as “miniature,” produce 88% of TC tornadoes ([Edwards et al. 2012](#)). These miniature supercells are dynamically and visually similar to Great Plains supercells, but are typically characterized by weaker reflectivities and rotational velocities ($<15 \text{ ms}^{-1}$), smaller mesocyclone diameters ($<7 \text{ km}$), shallower updrafts ($<10 \text{ km}$), and shorter life times (i.e., $<2 \text{ h}$; [Spratt et al. 1997](#); [McCaul and Weisman 1996](#); [Markowski and Straka 2000](#); [Suzuki et al. 2000](#); [Eastin and Link 2009](#); [Edwards et al. 2012](#)). Most of these miniature supercells occur in the rainbands of the northeastern quadrant of landfalling TCs during the day ([Novlan and Gray 1974](#); [McCaul 1991](#); [Schultz and Cecil 2009](#); [Edwards 2012](#)).

Corresponding author: Benjamin A. Schenkel, benschenkel@gmail.com

DOI: 10.1175/WAF-D-19-0220.1

© 2020 American Meteorological Society. For information regarding reuse of this content and general copyright information, consult the [AMS Copyright Policy](#) (www.ametsoc.org/PUBSReuseLicenses).

Moreover, $\sim 45\%$ of tornadoes in landfalling TCs occur within 50 km of the coast, with numbers rapidly decreasing with increasing coastal distance (McCaul 1991; Schultz and Cecil 2009; Edwards 2012). There is also large variability in the number of tornadoes among TCs with similar landfall locations and intensities, as exemplified by Hurricanes Ivan (2004) and Dennis (2005) shown in Fig. 1 (McCaul 1991; Baker et al. 2009; Edwards 2012).

Despite this prior work, our physical understanding of these aforementioned TC tornado characteristics remains incomplete. One understudied factor that may bridge these knowledge gaps is ambient (i.e., synoptic-scale) deep-tropospheric (i.e., 850–200-hPa) vertical wind shear (VWS; hereafter, VWS will refer to ambient deep-tropospheric values, as opposed to mid- or lower-tropospheric values), which has previously been hypothesized to impact tornado occurrence and location (McCaul 1991; Verbout et al. 2007; Green et al. 2011; Edwards 2012). Prior studies have shown that VWS is a dominant factor influencing convective symmetry and strength in TCs, both pre- and postlandfall (Corbosiero and Molinari 2002; Chen et al. 2006; Reasor et al. 2013). Moreover, previous research suggested that strong VWS is more frequently associated with favorable kinematic and thermodynamic environments for tornadoes (McCaul 1991; Molinari and Vollaro 2008, 2010; Molinari et al. 2012). Hence, the present study will analyze the relationship of VWS with TC tornadoes and their associated convective-scale environments.

TC tornadoes and their attendant supercells typically occur within environments characterized by modest thermodynamic instability and strong vertical wind shear (including directional shear) confined to the lower troposphere (McCaul 1991; McCaul and Weisman 1996, 2001). These favorable conditions allow for convective updrafts to efficiently tilt horizontal streamwise vorticity (i.e., horizontal vorticity parallel to flow) into the vertical, and stretch this newly created vertical vorticity yielding supercellular convection (Davies-Jones 1984; Wu et al. 1992; Drogemeier et al. 1993; McCaul and Weisman 1996). Several factors have been hypothesized to explain the existence of these environments:

- 1) The TC wind field veers and strengthens with height in the boundary layer due to friction, and veers and weakens with height above the boundary layer in association with TC warm-core structure, yielding favorable kinematic environments especially before the postlandfall weakening of the TC (Novlan and Gray 1974; Gentry 1983; Powell et al. 2003);

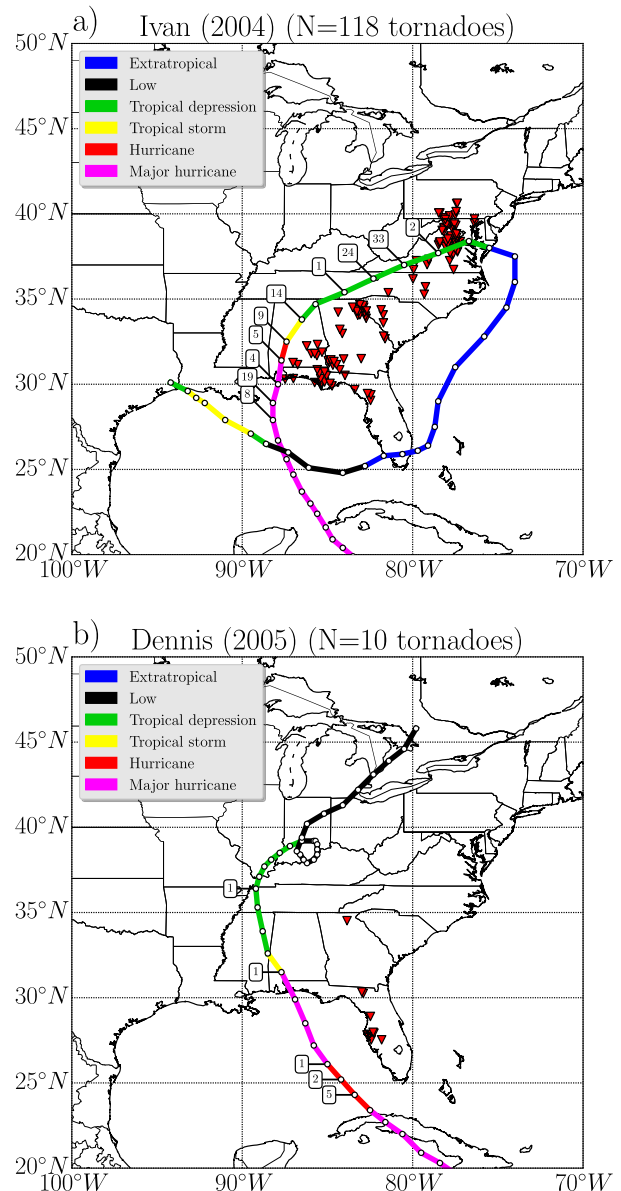


FIG. 1. Map view of tornado occurrence (red triangles), International Best Track Archive for Climate Stewardship (IBTrACS) TC track and intensity classification (e.g., colored by line segment; Knapp et al. 2010) for Hurricanes (a) Ivan (2004) and (b) Dennis (2005). The numbers within the boxes represent the number of tornadoes within ± 3 h of each IBTrACS TC time (connected via black line).

- 2) The convergent and cyclonic lower-tropospheric circulation of the TC may enhance frontogenesis associated with baroclinic boundaries (e.g., coastal fronts), providing a mesoscale source of lift, lower-tropospheric veering of the winds, and thermodynamic instability needed for tornadoes (Bosart and Dean 1991; Knupp et al. 2006; Green et al. 2011);
- 3) Continental, midtropospheric dry air intrusions into the TC may lead to evaporative cooling, stronger

- surface diabatic heating associated with convective suppression, and, ultimately, enhanced thermodynamic instability on the eastern half of the TC, where horizontal relative humidity gradients are strongest (Novlan and Gray 1974; McCaul 1987; Curtis 2004);
- 4) Diurnal surface heating may enhance thermodynamic instability over land in the more convectively sparse TC outer region or strengthen baroclinic boundaries near TCs due to horizontal cloud cover gradients (Knupp et al. 2006; Baker et al. 2009; Green et al. 2011).

While these factors play a role in tornado development in TCs, they likely do not fully explain why some TCs produce dozens of tornadoes and others produce very few (Fig. 1), and why tornadoes mostly occur in the northeastern quadrant of the TC—especially in inland environments.

One additional factor hypothesized to increase the potential for tornadoes in landfalling TCs is VWS, which has yet to be investigated for a large sample of cases (McCaul 1991; Verbout et al. 2007; Green et al. 2011; Edwards 2012). When VWS is moderate or strong, its impact on TC winds and convection is dominant over TC motion (Corbosiero and Molinari 2003; Chen et al. 2006; Abarca et al. 2011; Reasor et al. 2013), which does not strongly impact tornado frequency or location (McCaul 1991). Indeed, landfalling TCs often encounter strong VWS and produce tornado outbreaks during recurvature into the midlatitudes, typically in association with a trough embedded in the subtropical or polar jet (McCaul 1991; Corbosiero and Molinari 2003; Verbout et al. 2007; Edwards 2012). The 850–200-hPa layer is particularly relevant to TCs and their deep convection for several reasons: 1) the circulation and inner-core convection of a mature TC typically extend throughout the troposphere and, thus, are strongly impacted by vertical wind shear in this layer (Hawkins and Rubsam 1968; Frank 1977; Marks et al. 1992; Corbosiero and Molinari 2002), 2) TC intensity is typically strongly influenced by vertical wind shear within this layer (DeMaria and Kaplan 1994; Kaplan and DeMaria 2003; DeMaria et al. 2005; Kaplan et al. 2010), and 3) the vertical wind shear that TCs typically encounter is largest in the mid- to upper troposphere, in association with an upper-tropospheric trough (Frank 1982; Finocchio and Majumdar 2017; Rios-Berrios and Torn 2017).

Figure 2 shows a schematic demonstrating how weak (e.g., $<5 \text{ m s}^{-1}$) versus strong (e.g., $>10 \text{ m s}^{-1}$) VWS impacts the convective and wind field structure, and associated convective-scale kinematic and thermodynamic environments in TCs (Jones 1995; Frank and

Ritchie 1999; Corbosiero and Molinari 2002; Rios-Berrios and Torn 2017). TCs in weak VWS are vertically upright with a thermally direct secondary circulation (i.e., lower-tropospheric radial inflow, ascent at TC center, and upper-tropospheric radial outflow) that is approximately in thermal wind balance for steady-state TCs (Fig. 2a). In contrast, strongly sheared TCs are increasingly tilted with height in the direction of the VWS vector (i.e., downshear) due to differential advection by the ambient wind (Fig. 2b). This downshear tilting of the TC yields increasing cyclonic vorticity advection with height, compensating ascent, and an enhanced secondary circulation (Fig. 2b) in the downshear half of the TC as an adiabatically balanced response attempting to restore thermal wind balance (Raymond 1992; Jones 1995; Frank and Ritchie 1999; Reasor et al. 2004). Conversely, descent and deceleration of the TC secondary circulation occurs in the upshear half of the TC (Franklin et al. 1993; Frank and Ritchie 1999; Black et al. 2002; Molinari and Vollaro 2008). Perhaps most importantly, the enhancement of the TC secondary circulation downshear to a given VWS magnitude varies as a function of TC intensity, size, and latitude (Jones 1995; DeMaria 1996; Reasor et al. 2004; Reasor and Montgomery 2015). Each of these three aforementioned factors is also weakly correlated with one another (Merrill 1984; Chavas and Emanuel 2010; Chavas et al. 2016), suggesting that the response of the TC to a given magnitude of VWS varies depending on the structural characteristics of each cyclone. Stronger VWS is also associated with reduced intensification rates suggesting that the TC secondary circulation response to VWS may change over time (DeMaria 1996; DeMaria et al. 2005; Kaplan and DeMaria 2003).

Rather than simply being found downshear, the azimuthal location of the strongest ascent and deepest convection in moderately and strongly sheared cases varies with distance from the TC center. In the strongly convecting TC inner core, the lower half of the tilted TC circulation penetrates the upper half of the troposphere and cyclonically advects the upper portion of the TC to the left of the VWS vector in the downshear half of the TC (i.e., downshear left; Frank and Ritchie 1999). Hence, the strongest ascent and convection is also located downshear left in the TC inner core (e.g., Fig. 2d; Corbosiero and Molinari 2002, 2003; Chen et al. 2006; Stevenson et al. 2018). In contrast, the more convectively sparse TC outer region is associated with its strongest ascent and convection downshear and to the right of the VWS vector (i.e., downshear right; Fig. 2d; Corbosiero and Molinari 2002, 2003; Chen et al. 2006; Stevenson et al. 2016). This occurs in response to the adiabatic generation of a negative potential temperature

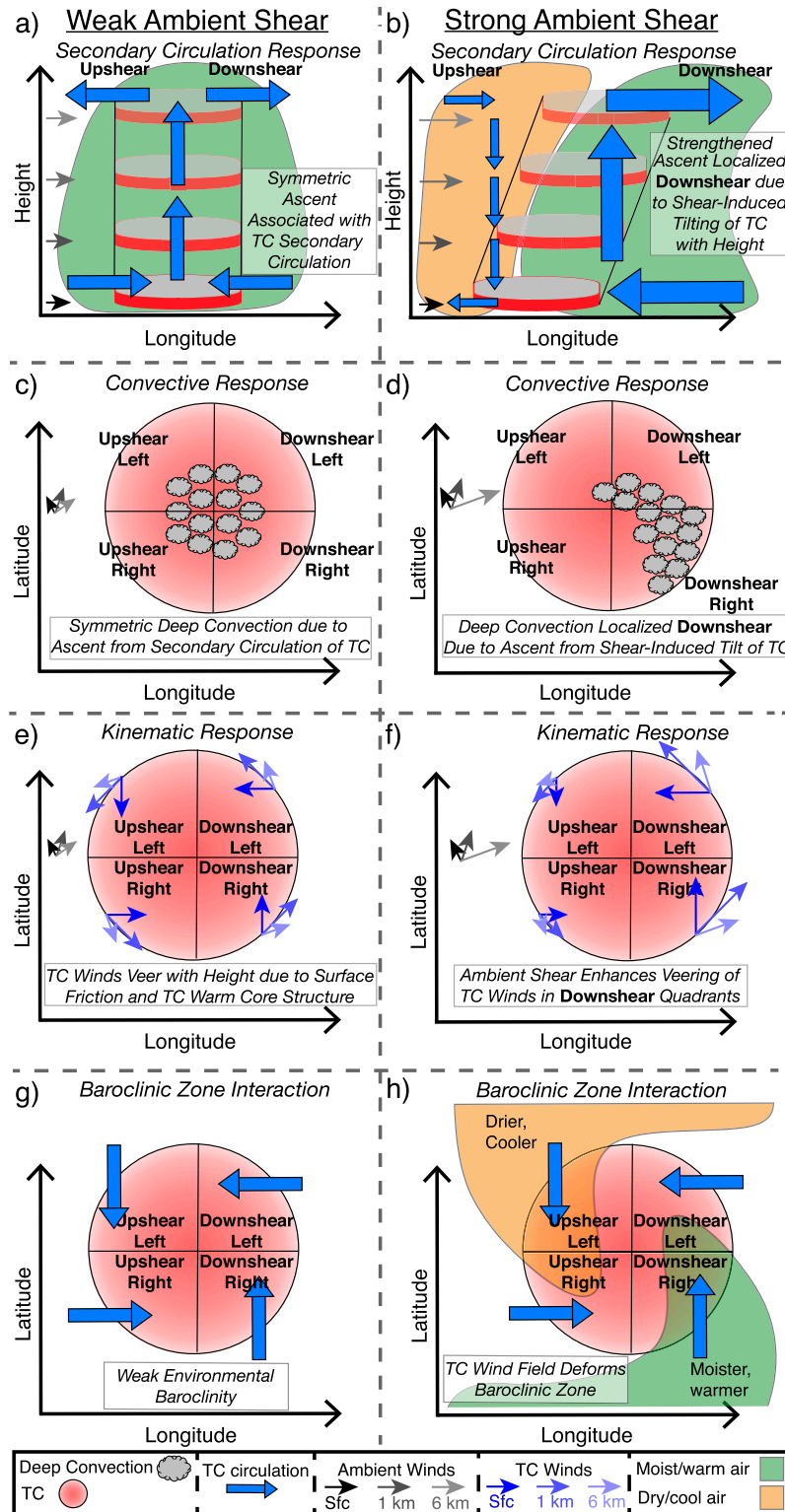


FIG. 2. Schematic showing response of TC to (left) weak vs (right) strong VWS including (a),(b) vertical cross sections of the TC secondary circulation response; (c),(d) plan view plots of deep convection location; (e),(f) plan view plots of the wind direction and magnitude (vector length) associated with the TC and its ambient environment; and (g),(h) plan view plots of the deformation of a baroclinic zone associated with weak and

anomaly downshear due to the VWS-induced enhanced ascent from the tilting of the TC, which causes parcels entering the downshear-right quadrant to isentropically ascend as they are cyclonically advected into this negative potential temperature anomaly (Jones 1995).

In addition to deep convection, favorable tornadic environments also occur in the downshear quadrants (Molinari and Vollaro 2008, 2010; Green et al. 2011) likely due to:

- *TC secondary circulation asymmetries*: Enhanced secondary circulation in the downshear half of the TC due to VWS yielding increased veering, and enhanced ascent, which moistens the troposphere (Figs. 2b,f; Franklin et al. 1993; Black et al. 2002; Molinari and Vollaro 2008);
- *Vector superposition*: Constructive superposition between veering of the ambient and TC winds that most strongly occurs in the downshear-right quadrant enhances the lower-tropospheric veering of the total wind field (i.e., environment plus TC) and nonlinearly increases its convective cell-relative helicity as VWS increases, all else being equal (Fig. 2f; Molinari and Vollaro 2008, 2010; Gu et al. 2018);
- *Baroclinic zone interaction*: Thermal wind balance suggests that strong VWS is associated with ambient baroclinicity, which is advected by the cyclonic circulation of the TC to yield moister, warmer air on its downshear half (Fig. 2h), especially during extratropical transition (i.e., ~50% of landfalling TCs eventually undergo transition; Jones 1995; Klein et al. 2000; Ritchie and Elsberry 2001; Hart and Evans 2001).

Additionally, any ambient source of cool, dry air (e.g., midtropospheric equivalent potential temperature minimum in tropics) can be efficiently fluxed into the downshear half of the TC inner core by mesoscale eddies that are generated by VWS-induced enhanced convection (Simpson and Riehl 1958; Tang and Emanuel 2010, 2012). In contrast to the downshear half of the TC, the upshear half of the TC is characterized by subsidence (and tropospheric drying) from the VWS-induced suppression of the TC secondary circulation, suppressed veering of the total wind field, and entrainment of drier, cooler ambient air from the ambient baroclinic zone. Moreover, the upshear dry anomalies in the lower troposphere have also been hypothesized to be from the

cyclonic advection of convective downdrafts from enhanced convection in the downshear half of the TC (Riemer et al. 2010; Reasor et al. 2013; Zhang et al. 2013; DeHart et al. 2014). Together, these conditions yield unfavorable conditions for tornadoes in the upshear half of the TC (Figs. 2a,c,e,g). Finally, these favorable conditions for tornadoes in the downshear half of strongly sheared TCs are more favorable than those typically found in weakly sheared TCs (Molinari and Vollaro 2008, 2010).

The response of the TC to VWS from prior work suggests that the largest number of tornadoes should occur in the downshear quadrants of strongly sheared TCs. To investigate this hypothesis, the present study conducts a statistical climatological analysis of VWS impacts upon the frequency, location, and convective-scale environments of tornadoes in TCs. We hypothesize that moderate-to-strong VWS influences both the frequency and location of tornadoes in TCs by providing both favorable kinematic and thermodynamic environments. We will use 24 years (1995–2018) of observed U.S. tornado and TC data together with reanalysis-derived VWS data to statistically analyze the relationship between tornado location and frequency with the magnitude and direction of VWS, similar to prior studies of deep convection (Corbosiero and Molinari 2002, 2003; Abarca et al. 2011). We will further provide physical insight into our results by analyzing convective-scale kinematic and thermodynamic environments using thousands of radiosondes in TCs. In particular, this study will address the following questions motivated by prior work:

- Is stronger VWS associated with greater numbers of tornadoes in TCs?
- Does VWS impact tornado location in landfalling TCs?
- Does VWS create favorable kinematic and thermodynamic environments for TC tornadoes?

2. Data and methods

a. TC and tornado data

The location, date, and damage ratings of tornadoes during landfalling TCs are obtained from the Storm Prediction Center (SPC) TC tornado dataset (TCTOR;

←

strong VWS as shown in prior work (Jones 1995; Frank and Ritchie 1999; Molinari and Vollaro 2008, 2010). The total wind field vectors (i.e., ambient plus TC) are not shown in (e) and (f), which instead show their subcomponents consisting of the ambient (black vectors) and the TC (blue vectors) winds plotted separately.

Edwards 2010). TCTOR spans from 1995 to 2018, which covers the period of enhanced tornado detection associated with the introduction of WSR-88D radars and the implementation of modern tornado warning and verification practices (Spratt et al. 1997; Edwards 2010). Each tornado report in TCTOR is subjectively analyzed from the full SPC tornado database to confirm its association with a TC using surface and upper air maps, archived satellite data, and radar data (Edwards 2010). Our analysis focuses on ambient conditions for each tornado and 6-h tornado frequency rather than tornado production over the entire lifetime of each TC since: 1) TC track data are reported at 6-h increments (Knapp et al. 2010) and 2) convective-scale environments in TCs can change rapidly over sub 6-h time periods due to changes in VWS (Rios-Berrios et al. 2016a,b; Nguyen et al. 2017; Ryglicki et al. 2018), and land interaction (Emanuel 1986; Kaplan and DeMaria 1995; DeMaria et al. 2005).

TC data from 1995 to 2018 are obtained from the National Hurricane Center as provided in version 4, revision 0 of the International Best Track Archive for Climate Stewardship (IBTrACS; Knapp et al. 2010). We consider a TC as capable of producing a tornado for a given 6-h time if the TC is classified as tropical (i.e., not subtropical or extratropical), and it occurs within 750 km of the U.S. coast. A 750-km distance is chosen for consistency with the radius from the TC over which nearly all (>99%) tornadoes occur (Pearson and Sadowski 1965; Novlan and Gray 1974; Schultz and Cecil 2009; Edwards 2010). For each tornado, TC track data are temporally interpolated to the time of tornado start using a piecewise cubic Hermite polynomial, which eliminates overestimates that can occur during spline interpolation (Chavas et al. 2016; Schenkel et al. 2017).

b. VWS data

The 6-h $0.25^\circ \times 0.25^\circ$ European Centre for Medium-Range Weather Forecasts (ECMWF) fifth-generation reanalysis (ERA5) available from 1980 to 2018 (Hersbach et al. 2020) is used to calculate VWS. Prior studies have shown that reanalysis TC track, outer size and structure, and their environment are well represented, especially near observation-dense areas like the continental United States (Schenkel and Hart 2012; Murakami 2014; Hodges et al. 2017; Schenkel et al. 2017). Moreover, reanalyses have also been extensively used to calculate VWS for TCs in prior work (Tang and Emanuel 2012; Tang and Camargo 2014; Finocchio and Majumdar 2017; Rios-Berrios and Torn 2017).

VWS is calculated by computing the areal-averaged 850–200-hPa vertical wind shear (with the TC wind field removed) for each 6-h IBTrACS data point in three steps (Davis et al. 2008; Galarneau and Davis 2013;

Rios-Berrios and Torn 2017): 1) computing the irrotational and nondivergent wind components associated with the TC by solving the Poisson equation for streamfunction and velocity potential, using homogeneous boundary conditions within a 500-km radius from the TC center at 850 and 200 hPa, 2) subtracting the irrotational and nondivergent components of the TC from the total wind field at each pressure level, and 3) subtracting the 850-hPa wind vectors from those at 200 hPa to compute the vertical wind shear, and average the resulting shear within a 500-km radius from the TC center. A 500-km radius is chosen due to its use in prior analyses of VWS impacts on TCs (Corbosiero and Molinari 2002, 2003; Galarneau and Davis 2013; Rios-Berrios and Torn 2017), its consistency with the approximate median size of the TC outer wind field (Chavas and Emanuel 2010; Chavas et al. 2016; Schenkel et al. 2017, 2018), and due to the majority of tornadoes being located within 500 km of the TC center (Novlan and Gray 1974; Schultz and Cecil 2009; Edwards 2012). We then temporally interpolate VWS for the 6-h IBTrACS TC data to the time of tornado occurrence using a piecewise cubic Hermite polynomial. VWS for each TC is classified into three categories based upon terciles of VWS distribution that includes all Atlantic TCs similar to prior work (Rios-Berrios and Torn 2017; Ditchek et al. 2019):

- 1) Strong (upper 33rd percentile): $>11.2 \text{ m s}^{-1}$;
- 2) Moderate (middle 33rd percentile): $6.7\text{--}11.2 \text{ m s}^{-1}$;
- 3) Weak (bottom 33rd percentile): $<6.7 \text{ m s}^{-1}$.

These categories are coincidentally similar to previously chosen empirical thresholds shown to impact deep convection in TCs (Corbosiero and Molinari 2002, 2003; Molinari and Vollaro 2008). Table 1 shows the number of tornadoes and associated uniquely named TCs in each VWS regime.

c. Radiosonde data

We compute severe convective weather kinematic and thermodynamic metrics from radiosonde data to diagnose the environmental favorability for tornadoes in TCs. These soundings are *not* tornado proximity soundings. Very few proximity soundings (Potvin et al. 2010; Edwards and Thompson 2012) exist due to the challenges of observing the short life cycle of TC tornadoes (Spratt et al. 1997; McCaul and Weisman 1996; Eastin and Link 2009) and the dangers posed by other landfalling TC hazards. Rather this analysis examines a large sample of radiosondes to statistically analyze whether interactions between VWS and the TC may support tornadic environments. Radiosondes are taken from the National Oceanographic and Atmospheric

TABLE 1. Sample sizes of tornadoes and uniquely named TCs producing tornadoes in strong, moderate, and weak VWS. The same TC may contribute multiple 6-h times to each VWS regime such that the sum of the number of TCs in the strong, moderate, and weak VWS categories does not equal the number in the all VWS category.

	No. of tornadoes	No. of TCs
All VWS	1275	86
Strong VWS	685	61
Moderate VWS	378	51
Weak VWS	212	31

Administration (NOAA) Integrated Global Radiosonde Archive (IGRA), version 2, which is a global, multi-decadal radiosonde archive (Durre et al. 2006). The IGRA uses several tests to check the physical and internal consistency of radiosondes. To ensure each radiosonde has sufficient data, we exclude the soundings if wind, temperature, or moisture data are missing (Molinari and Vollaro 2008, 2010): 1) within 200 m of the surface or 2) over a layer ≥ 1 km below a height of 8 km. Radiosondes launched within 75 km of the TC center are also excluded, to remove soundings with large cyclone-relative azimuthal displacements due to advection by the TC circulation, since the vertical profiles do not represent a single, local column (Molinari and Vollaro 2010). We also only consider radiosondes within 750 km of the TC center, to be consistent with the radius of most frequent tornado occurrence (e.g., Schultz and Cecil 2009). These criteria leave us with 8001 radiosondes in 222 Atlantic TCs from 1995 to 2018 within the United States, Central America, and the Caribbean. Table 2 shows the number of radiosondes and uniquely named TCs sampled in each VWS regime. The VWS-relative locations of radiosondes for strongly, moderately, and weakly sheared TCs are shown in Fig. 3.

To quantify the kinematic environmental favorability for tornadoes in TCs, we compute 0–3- and 0–1-km convective cell-relative helicity from radiosondes (Davies 1990):

$$\text{SREH} = \int_0^h \left[(\mathbf{v} - \mathbf{c}) \cdot \left(\mathbf{k} \times \frac{\partial \mathbf{v}}{\partial z} \right) \right] dz, \quad (1)$$

where \mathbf{v} is the measured wind vector, \mathbf{c} represents the convective cell motion vector, and h is the layer depth (i.e., 3 or 1 km). In a Cartesian coordinate, the horizontal variation in the curvature of the wind field artificially contributes to the helicity measured by radiosondes as they are cyclonically advected around the TC, which can inflate helicity by 5%–8% (Yamei and Rongsheng 2003; Molinari and Vollaro 2008, 2010). However, like prior radiosonde analyses of TC tornadoes, we acknowledge and retain these uncertainties as the absence of

geolocation data at every level precludes their removal (McCaul 1987, 1991; Baker et al. 2009).

Both 0–3- and 0–1-km layers are examined since enhanced lower-tropospheric helicity primarily concentrated near the surface is useful in discriminating between tornadic and nontornadic convection (Rasmussen 2003; Markowski et al. 2003; Thompson et al. 2003). Convective cell motion is computed using the method of Bunkers et al. (2000) with a modification similar to Ramsay and Doswell (2005), used in the absence of cell motion from radar data. This method computes the convective-cell motion as being equal to the pressure-weighted mean wind between 0 and 8 km, with the addition of a component with a magnitude of 7.5 m s^{-1} that is 90° clockwise to the 0–6-km layer vertical wind shear vector direction calculated from radiosondes (Ramsay and Doswell 2005). Our analysis also presents composite median TC-relative tangential and radial winds, and hodographs computed from the radiosondes and reanalyses, which are transformed into a vertical coordinate that accounts for surface elevation differences among radiosonde sites (Gal-Chen and Somerville 1975; Parker 2014):

$$z^* = H \frac{z - z_{\text{sfc}}}{H - z_{\text{sfc}}}, \quad (2)$$

where H is the tropopause height assumed to be 12 km and z_{sfc} is the sounding station altitude. All heights on the right-hand side are above mean sea level. All radiosondes are vertically interpolated to this coordinate with a 100-m interval using a piecewise cubic Hermite polynomial. Similar to helicity, lower-tropospheric TC-relative radial and tangential winds may also contain errors that cannot be removed due to the absence of geolocation data at every vertical level (not shown), although these errors are likely below the instrument precision and absolute accuracy (e.g., Hock and Franklin 1999).

The thermodynamic environmental favorability for tornadoes in TCs is analyzed using 0–3-km convective available potential energy (CAPE) and median skew T –log p diagrams computed from radiosonde data. We assume a 200-m mixed layer for CAPE calculations similar to the recommendations for tropical deep convection and TCs (Roms and Kuang 2011; Molinari et al. 2012). Both lower-tropospheric kinematic and thermodynamic parameters are computed because 1) buoyancy and wind are maximized in the lower troposphere for convective-scale environments in TCs (McCaul 1991; Molinari and Vollaro 2008; Baker et al. 2009) and 2) tornadic supercells are shallower in TCs compared to the Great Plains (Spratt et al. 1997; McCaul and Weisman 1996; Baker et al. 2009; Eastin and Link 2009).

TABLE 2. Number of radiosondes and uniquely named TCs sampled by radiosondes in all cases and those in strong, moderate, and weak VWS. The same TC may be sampled by multiple radiosondes such that the number of TCs sampled by radiosondes in strong, moderate, and weak VWS will not equal the number in the all VWS category.

	No. of radiosondes	No. of TCs sampled by radiosondes
All VWS	8001	222
Strong VWS	2889	160
Moderate VWS	3172	165
Weak VWS	1940	117

d. Statistical significance methodology

To objectively determine the differences between two distributions, we use a 1000-sample bootstrap approach, with replacement, for a two-tailed test at the 95% confidence interval, to determine the differences between their medians. We also employ a 1000-sample bootstrap approach to determine whether Pearson correlation coefficients are statistically different from 0 by randomly resampling the distribution 1000 times, computing a correlation coefficient for each distribution iteration, and comparing the 95% confidence interval of

the resulting correlation coefficient distribution. In the interest of brevity, we will state that two distributions exhibit statistically significant differences from one another if the test criterion is satisfied at the 95% confidence interval, rather than stating the p values each time. Statistical significance testing is used to quantify differences in kinematic and thermodynamic quantities from radiosondes, and differences in VWS between TCs with differing 6-h tornado production.

3. Analysis and results

a. Tornado number and damage category

A comparison of tornado number in each damage category stratified by strong, moderate, and weak VWS (Fig. 4) shows that, regardless of their damage category, the largest fraction of tornadoes occur in strongly sheared TCs. Specifically, 54% of all tornadoes occur in strongly sheared TCs compared to only 30% and 16% of tornadoes in moderately and weakly sheared TCs, respectively. Strongly sheared TCs also produce a larger fraction of more damaging tornadoes, including 80% of EF2+/F2+ and 63% of EF1/F1 cases compared to 47% of EF0/F0.

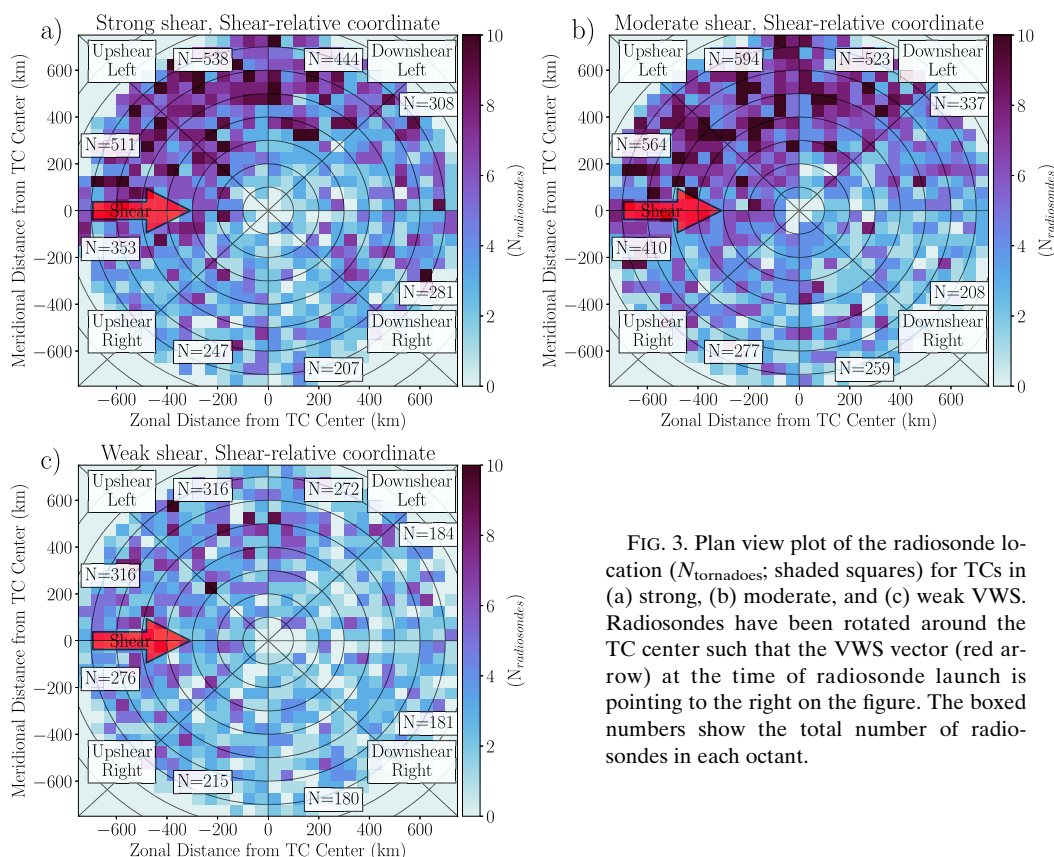


FIG. 3. Plan view plot of the radiosonde location ($N_{\text{tornadoes}}$; shaded squares) for TCs in (a) strong, (b) moderate, and (c) weak VWS. Radiosondes have been rotated around the TC center such that the VWS vector (red arrow) at the time of radiosonde launch is pointing to the right on the figure. The boxed numbers show the total number of radiosondes in each octant.

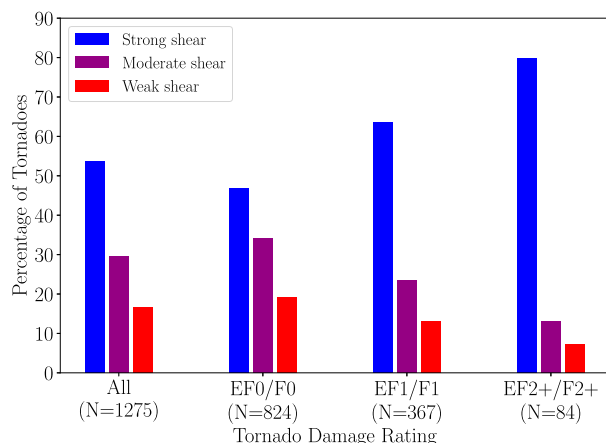


FIG. 4. Bar plots of tornado damage rating category (enhanced Fujita or Fujita scale) in TCs stratified by the VWS category. Each bar plot is expressed as a percentage of the number of tornadoes for each VWS regime relative to the total number of tornadoes produced in the given damage rating category. The sample sizes along the x axis show the total number of tornadoes for each tornado damage rating category.

The larger fraction of tornadoes that occur in strongly sheared TCs is due to enhanced tornado production, especially higher-end tornado events, rather than TCs occurring more often in strongly sheared environments. To demonstrate this, the percentage of tornadoes per 6 h for TCs, stratified by VWS category, is shown in Fig. 5. TCs near the U.S. coast occur in moderate VWS most frequently (925) compared to either strong (894) or weak VWS (672), consistent with prior work (Corbosiero and Molinari 2002, 2003). The larger number of tornadoes in strongly sheared TCs (Fig. 4) is due to a greater number of 6-h times with 5+ tornadoes in strongly sheared TCs (58% of all 5+ events) compared to either moderately (28%) or weakly (14%) sheared TCs (Verbout et al. 2007). In contrast, strongly sheared TCs constitute a similar percentage of 6-h times with 1–2 (45%) and 3–4 (39%) tornadoes compared to moderately sheared TCs (38% and 39% for 1–2 and 3–4 tornadoes, respectively), while weakly sheared TCs are less productive. Considering these results together, 19% of all 6-h times for strongly sheared TCs are associated with 1+ tornadoes, compared to 14% and 10% of 6-h times for moderately and weakly sheared TCs.

To show that the association between VWS and higher-end TC tornado production is not an artifact of using three VWS bins, Fig. 6a shows distributions of VWS conditioned on the number of tornadoes per 6 h. Indeed, the distribution of 5+ tornadoes per 6 h is shifted toward stronger VWS in comparison to the remaining three distributions of 6-h tornado production. In particular, the difference between the median VWS

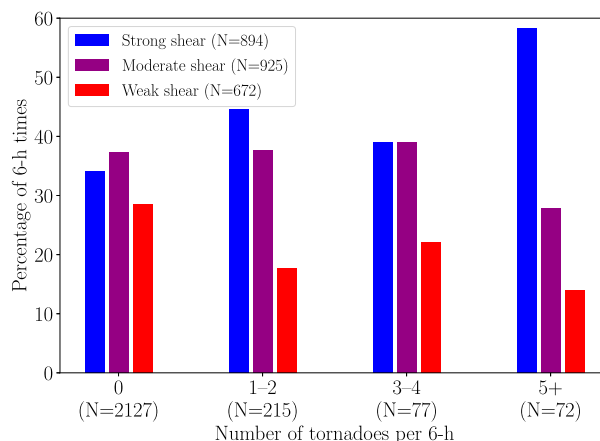


FIG. 5. Bar plots of tornado production per 6 h in TCs stratified by VWS category for a given category of tornado production (%) for all TCs within 750 km of the U.S. mainland. Each bar plot is expressed as a percentage of the number of 6-h times for a given VWS regime relative to the total number of 6-h times for a given threshold of tornado production. The sample size along the x axis shows the total number of 6-h times for each tornado production threshold, while the legend shows the total number of 6-h times in each VWS regime.

values for TCs producing 0 and 5+ tornadoes per 6 h is 3.1 m s^{-1} , which is statistically different at the 95% confidence interval, as implied by Verbout et al. (2007). Stronger VWS is typically associated with enhanced lower-tropospheric convective-cell relative helicity (Molinari and Vollaro 2008, 2010; Nolan 2011; Onderlinde and Nolan 2014), which has been identified as one of several potential discriminants between outbreaks and nonoutbreaks in both TC and non-TC events (McCaul 1991; Verbout et al. 2007; Shafer et al. 2010; Mercer et al. 2012). Additionally, the whiskers for the 5+ tornadoes per 6 h category also do not extend past 19 m s^{-1} . This VWS threshold is typically associated with TC weakening and the disruption of its convective structure (Paterson et al. 2005; Hendricks et al. 2010). These results may suggest that VWS between 10 and 19 m s^{-1} is an ideal range in which the VWS-induced kinematic environmental favorability (Molinari and Vollaro 2008, 2010) outweighs the weakening of the TC due to VWS.

TCs with enhanced 6-h tornado production also tend to occur in VWS with a stronger southerly component, as shown in circular histograms (Fig. 6b). Regardless of 6-h tornado production, Fig. 6b shows that 88% of TCs occur in westerly VWS (Corbosiero and Molinari 2003). As tornado production increases, the VWS distribution narrows and becomes more southwesterly, as expected from Verbout et al. (2007). As an example, the median values of VWS direction for TCs that produce 0 versus 5+ tornadoes per 6 h are 272° (westerly) and 242°

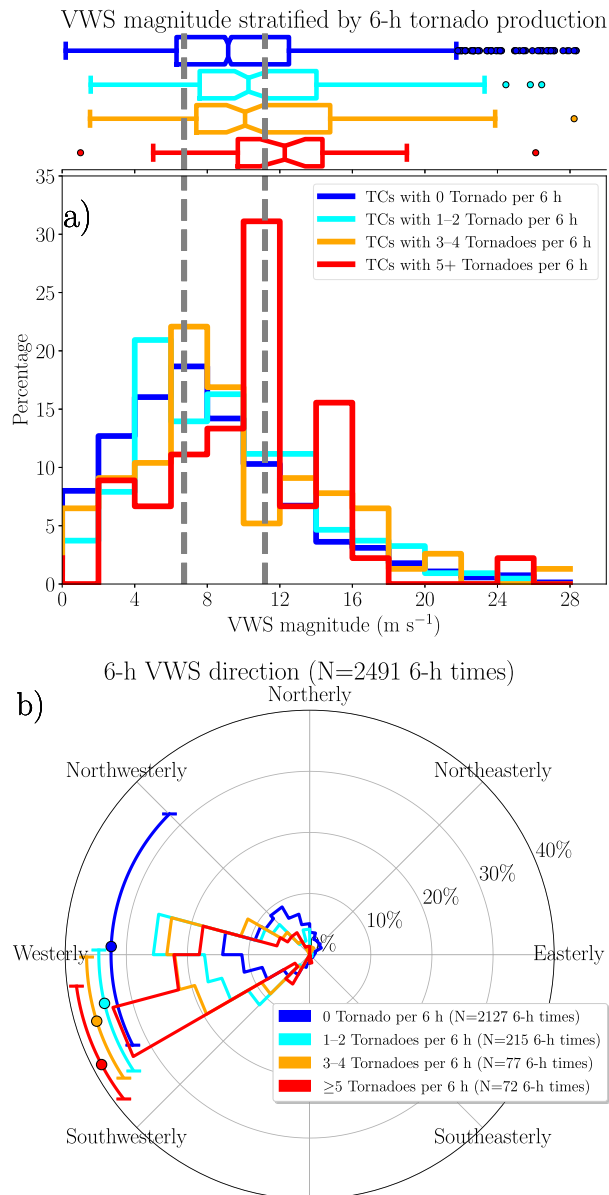


FIG. 6. (a) Bar plot (%) and box-and-whisker plot of 6-h VWS magnitude (m s^{-1}) and (b) circular bar plot (%) of median (filled circle) and interquartile range (whiskers) of 6-h VWS direction stratified by 6-h TC tornado production for all TCs within 750 km of the U.S. mainland. The bar plots are expressed as a percentage of the number of total observations for each category of 6-h tornado production. The gray dashed vertical lines in (a) denote the lower and upper 33rd percentiles of VWS used to define weak, moderate, and strong VWS. The box plots in (a) display the median (vertical lines near box center), the 95% confidence interval of the median calculated from a 1000-sample bootstrap approach with replacement (notches on boxes), the interquartile range (box perimeter; $[q_1, q_3]$), whiskers [horizontal lines extending from box perimeter; $[q_1 - 1.5(q_3 - q_1), q_3 + 1.5(q_3 - q_1)]$], and outliers (filled circles).

(southwesterly), respectively, which are statistically different at the 95% confidence interval.

Together, these results suggest that tornadoes more frequently occur in TCs embedded in stronger, more southwesterly VWS. However, too strong of VWS may be unfavorable. These results imply that variations in VWS explain 6-h tornado production variability, especially for higher-end events. However, the occurrence of tornadoes in weakly sheared TCs also more generally suggests that VWS is certainly not the sole factor influencing tornado production.

b. Cyclone-relative location of tornadoes

Comparison of tornado location using plan view, VWS-relative plots in the three VWS regimes (Figs. 7a,c,e) shows that tornadoes are increasingly confined to the downshear half of TCs as VWS strengthens. Approximately, 76%, 87%, and 97% of tornadoes occur in the downshear half in weakly, moderately, and strongly sheared TCs, consistent with prior work on deep convection (Corbosiero and Molinari 2002, 2003; Chen et al. 2006). More specifically, tornadoes primarily cluster in the two octants directly downshear in TCs within strong (79%), moderate (72%), and weak (52%) VWS. Similar plots of tornado locations in a true north coordinate (Figs. 7b,d,f) show that tornadoes are less strongly clustered in the northeast quadrant compared to the two downshear octants in the VWS-relative plots. In strongly sheared TCs, the VWS-relative location of maximum tornado frequency is downshear left in the inner core before transitioning with increasing radius to downshear right, similar to analyses of deep convection (Corbosiero and Molinari 2002, 2003; Chen et al. 2006). In contrast, the radial dependence of azimuthal tornado location is weaker in the true-north-relative plots, transitioning from the north-northeast octant to the east-northeast octant between inner and outer radii, respectively. For weak or moderate VWS regimes, tornadoes are more loosely clustered primarily directly downshear at all radii, while also occasionally occurring in the upshear-left quadrant, similar to prior work on deep convection (Corbosiero and Molinari 2002, 2003; Chen et al. 2006).

The results from Fig. 7 are distilled into a single plot showing tornado location as a function of both VWS magnitude and VWS-relative sector (Fig. 8). Tornadoes can occur in any VWS-relative quadrant under weak VWS, albeit less frequently. In these weakly sheared regimes, the location of tornadoes may be more strongly influenced by TC motion, with right-of-motion potentially favored due to constructive superposition between the TC and its ambient steering flow. This superposition yields enhanced near-surface frictional convergence, and longer hodographs associated with

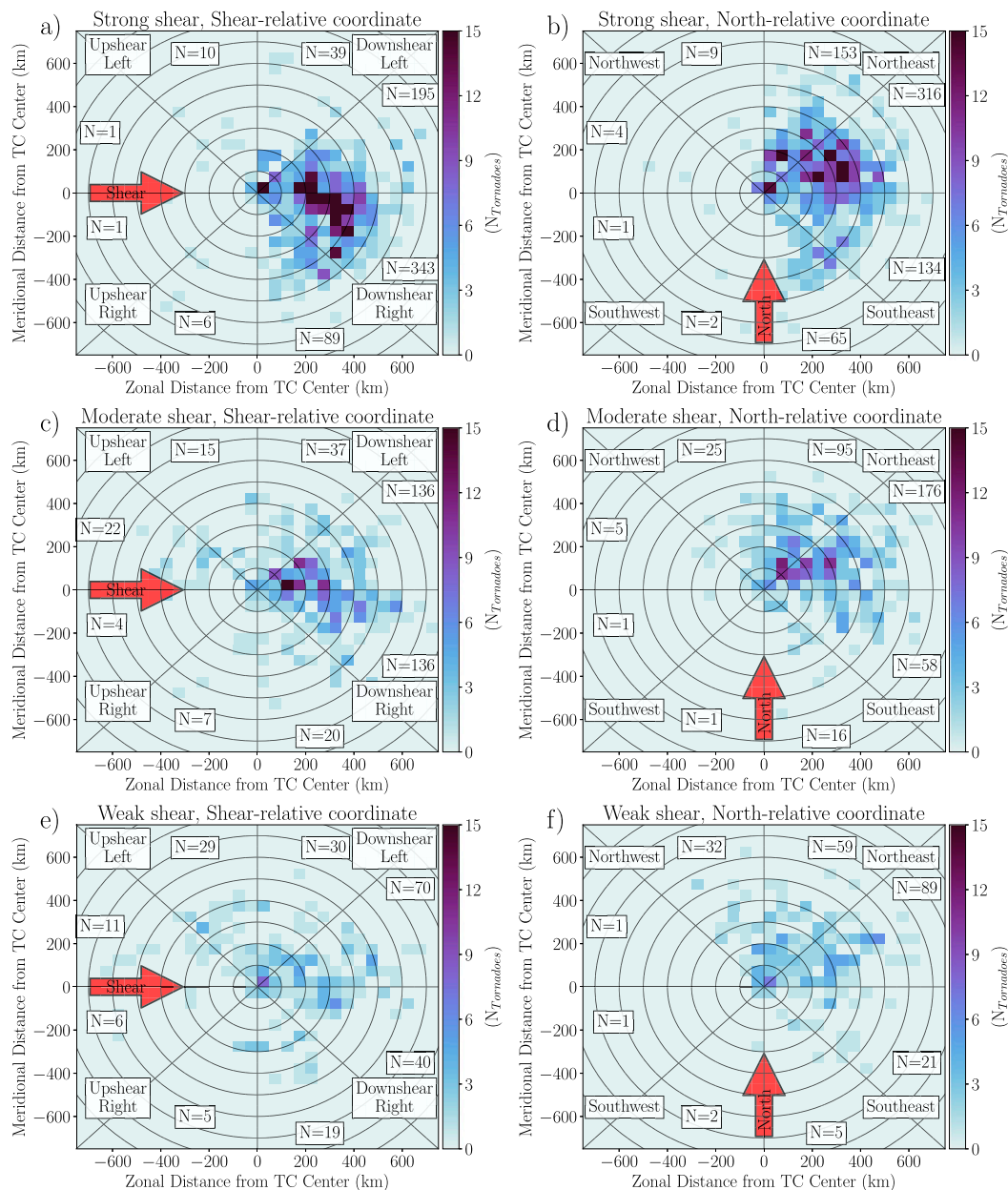


FIG. 7. Plan view plot of tornado location ($N_{\text{tornadoes}}$; shaded squares) for TCs in (a),(b) strong; (c),(d) moderate; and (e),(f) weak VWS. Tornado reports in (a), (c), and (e) have been rotated around the TC center such that the VWS vector (red arrow) at the time of tornado occurrence is pointing to the right. The tornado reports in (b), (d), and (f) are plotted relative to true north with the red arrow labeled accordingly. The boxed numbers show the total number of tornadoes in each octant.

larger ground-relative winds (Shapiro 1983; Bender 1997; Frank and Ritchie 1999; Corbosiero and Molinari 2003). However, as VWS increases, tornadoes both occur more frequently and are increasingly localized to the downshear half of the TC, including nearly all tornadoes in strongly sheared regimes. This result suggests the dominance of strong VWS over other factors (e.g., TC

motion; Corbosiero and Molinari 2003; Chen et al. 2006; Ueno 2007; Wingo and Cecil 2010).

These results suggest an association between the VWS-relative sector and VWS magnitude that is consistent with prior studies of deep convection in TCs (Corbosiero and Molinari 2002, 2003; Chen et al. 2006). Moreover, VWS may provide a physical explanation for

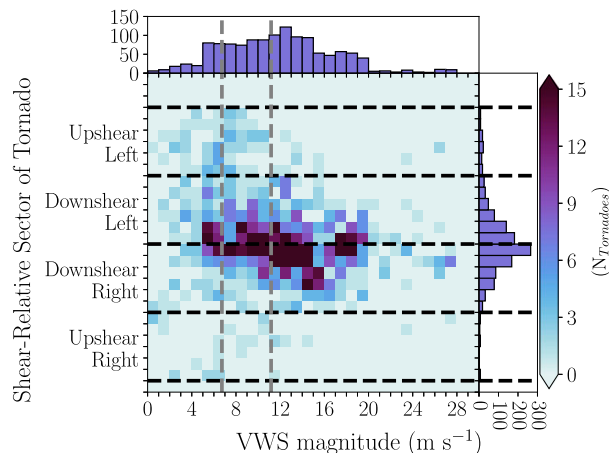


FIG. 8. Joint histogram of VWS magnitude (m s^{-1}) vs the VWS-relative sector of tornado location for all tornadoes (shaded squares; $N_{\text{tornadoes}}$). The one-dimensional histograms on top and to the right show VWS magnitude and tornado sector relative to the VWS direction, respectively. The horizontal black dashed lines show the boundaries between VWS-relative sectors, and the vertical gray dashed lines show the boundaries between strong, moderate, and weak VWS.

why tornadoes often occur in the northeastern quadrant of the TC, which is typically the two sectors located directly downshear. To better understand the association between VWS and tornadoes, an analysis of convective-scale data from radiosondes is presented in the next section.

c. Kinematic environments

The distributions of 0–3-km convective cell-relative helicity at each radius from the TC center for the three VWS regimes (Fig. 9) shows the kinematic favorability for tornadic supercells in TCs. Helicity increases only in the downshear-right quadrant as VWS strengthens (Molinari and Vollaro 2008, 2010). In particular, median 0–3-km convective-cell relative helicity values at radii between 300 and 600 km in the downshear-right quadrant are approximately 2–3 times larger in strongly sheared TCs than for TCs in weak or moderate VWS, with median values that are statistically different at the 95% confidence interval. Moreover, median helicity values in the downshear-right quadrant within a 500-km radius of strongly sheared TCs falls within the range typically associated with midlatitude tornadic supercells (i.e., $100\text{--}280 \text{ m}^2 \text{ s}^{-2}$; Rasmussen and Blanchard 1998; Thompson et al. 2003; Houston and Wilhelmson 2007). Helicity in the downshear-right quadrant of strongly sheared TCs is also larger than other VWS-relative quadrants, generally between 300 and 500 km from the TC center, where median values are statistically different at the 95% confidence interval. In contrast, weakly

and moderately sheared TCs are associated with median 0–3-km convective cell-relative helicity that is generally below the range associated with tornadic supercells, and reduced asymmetries in helicity among the VWS-relative quadrants (Molinari and Vollaro 2008, 2010).

The nonlinear dependence of 0–3-km convective cell-relative helicity upon VWS is shown next (Fig. 10) by aggregating all radiosondes from TC radii with helicity shown to be sensitive to VWS (i.e., radius ≤ 500 km) in each quadrant. In particular, a moderate Pearson correlation coefficient ($R = 0.46$; and statistically different from 0 at the 95% confidence interval) in the downshear-right quadrant is suggestive of nonlinearity. More specifically, median helicity only statistically changes between the transition from moderate to strong VWS regimes. As previously mentioned, this nonlinearity is consistent with 1) constructive superposition of the ambient and TC winds in the downshear-right quadrant and 2) VWS-induced enhancement of the TC secondary circulation downshear. With regards to the first factor, increased ambient VWS is typically associated with increased layer-mean winds and horizontal vorticity (Finocchio and Majumdar 2017; Rios-Berrios and Torn 2017), which will yield a nonlinear enhancement of helicity given its dependence on both of these terms [Eq. (1)], even if the TC winds remain unchanged. However, prior work has shown that TC intensification rates are also typically reduced as VWS increases (DeMaria and Kaplan 1994; Kaplan and DeMaria 2003; DeMaria et al. 2005), which suggests that the helicity of the TC wind field may simultaneously decrease. For the second factor, the downshear enhancement of the TC secondary circulation to a given magnitude of VWS is nonlinearly dependent on TC intensity, size, and latitude, suggesting that the response depends on the characteristics of each individual TC (Jones 1995; Reasor et al. 2004; Reasor and Montgomery 2015). Last, the remaining VWS-relative quadrants do not show statistical increases in helicity with stronger VWS.

Distributions of 0–1-km convective cell-relative helicity are shown next (Fig. 11) to further distinguish between tornadic and nontornadic near-surface supercell environments. Typically, 0–1-km convective cell-relative helicity (Fig. 11) is at least $\sim 50\%$ of the magnitude of 0–3-km helicity (Fig. 9), which is typical of tornadic supercell environments (Thompson et al. 2003; Markowski et al. 2003; Rasmussen 2003). Similar to the 0–3-km layer, the downshear-right quadrant of strongly sheared TCs is the only quadrant with median 0–1-km helicity well within the range associated with tornadic supercells at all radii within 700 km of the TC center (i.e., $33\text{--}210 \text{ m}^2 \text{ s}^{-2}$; Thompson et al. 2003; Rasmussen

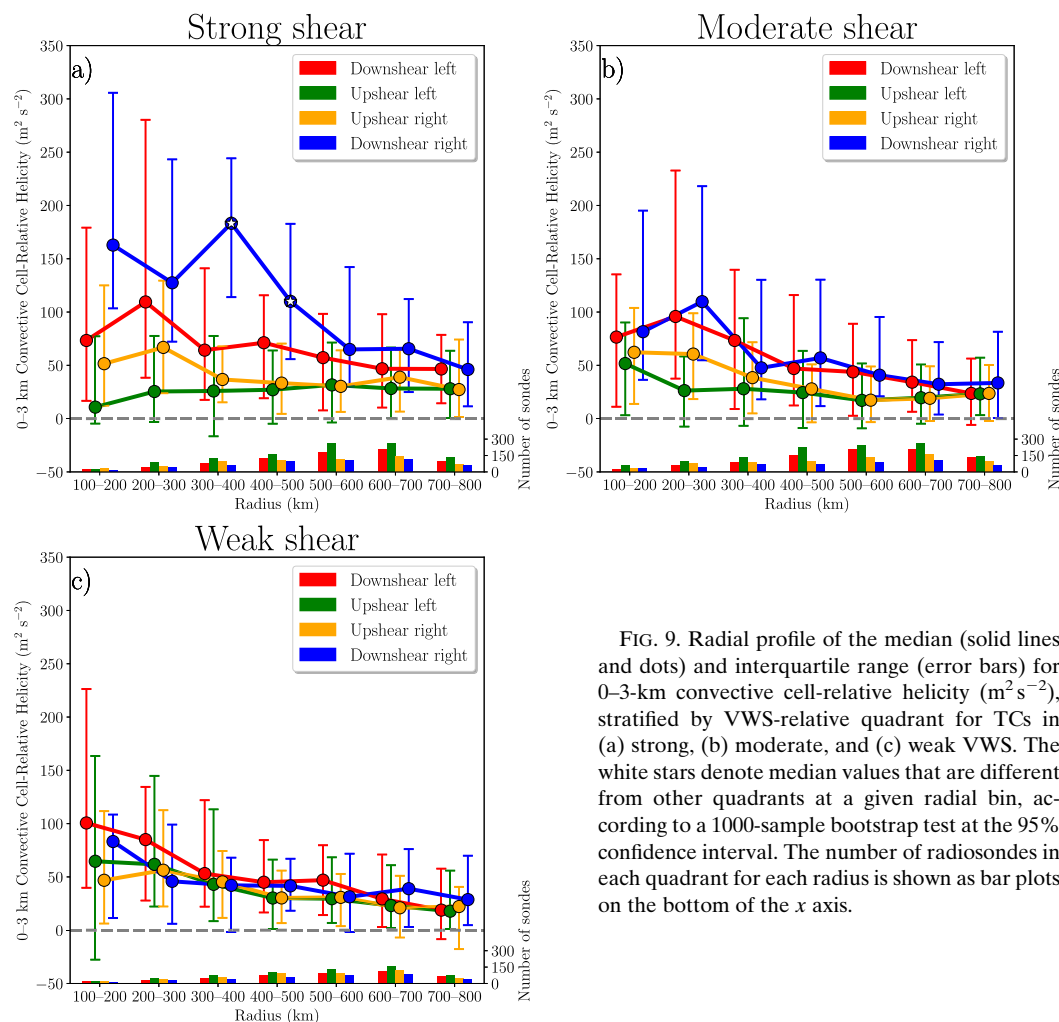


FIG. 9. Radial profile of the median (solid lines and dots) and interquartile range (error bars) for 0–3-km convective cell-relative helicity ($\text{m}^2 \text{s}^{-2}$), stratified by VWS-relative quadrant for TCs in (a) strong, (b) moderate, and (c) weak VWS. The white stars denote median values that are different from other quadrants at a given radial bin, according to a 1000-sample bootstrap test at the 95% confidence interval. The number of radiosondes in each quadrant for each radius is shown as bar plots on the bottom of the x axis.

2003; Houston and Wilhelmson 2007). Finally, helicity in the downshear-right quadrant of strongly sheared TCs is both larger than the helicity in: 1) the downshear-right quadrant of weakly and moderately sheared TCs and 2) all three remaining VWS-relative quadrants regardless of VWS magnitude. This is borne out by statistical differences at the 95% confidence interval between the median values of these distributions.

Composite median hodographs are presented to show the vertical structure of the convective-scale kinematic environment with the estimated cell motion denoted (Fig. 12). The downshear-right quadrant hodograph in strongly sheared TCs is dominated by strong speed shear in the lowest 1 km, with directional shear immediately above that level (Molinari and Vollaro 2008, 2010; Gu et al. 2018), typical of tornadic supercell environments (Brown et al. 1973; Markowski et al. 2003; Thompson et al. 2003). Moreover, winds are strongest throughout the troposphere in the downshear-right quadrant likely

due to constructive superposition between the TC and ambient winds and VWS-induced enhancement of the TC secondary circulation (Jones 1995; Frank and Ritchie 1999; Molinari and Vollaro 2010). In contrast, the downshear-left quadrant hodograph has comparatively weaker near-surface speed shear in strongly sheared TCs (Molinari and Vollaro 2010; Gu et al. 2018), while the two upshear quadrants are characterized by more marginal speed and directional shear. Compared to TCs in strong VWS, weakly and moderately sheared TCs (Figs. 12b,c) have shorter, vertically stacked hodographs in each VWS-relative quadrant. Finally, the increasing hodograph length above 6 km in the upshear-left and downshear-left quadrants in stronger VWS regimes, with a southwesterly direction (Fig. 6b), implies a stronger westerly jet to the northwest of the TC (Verbout et al. 2007).

We next decompose the radiosonde data into composite median lower-tropospheric cyclone-relative

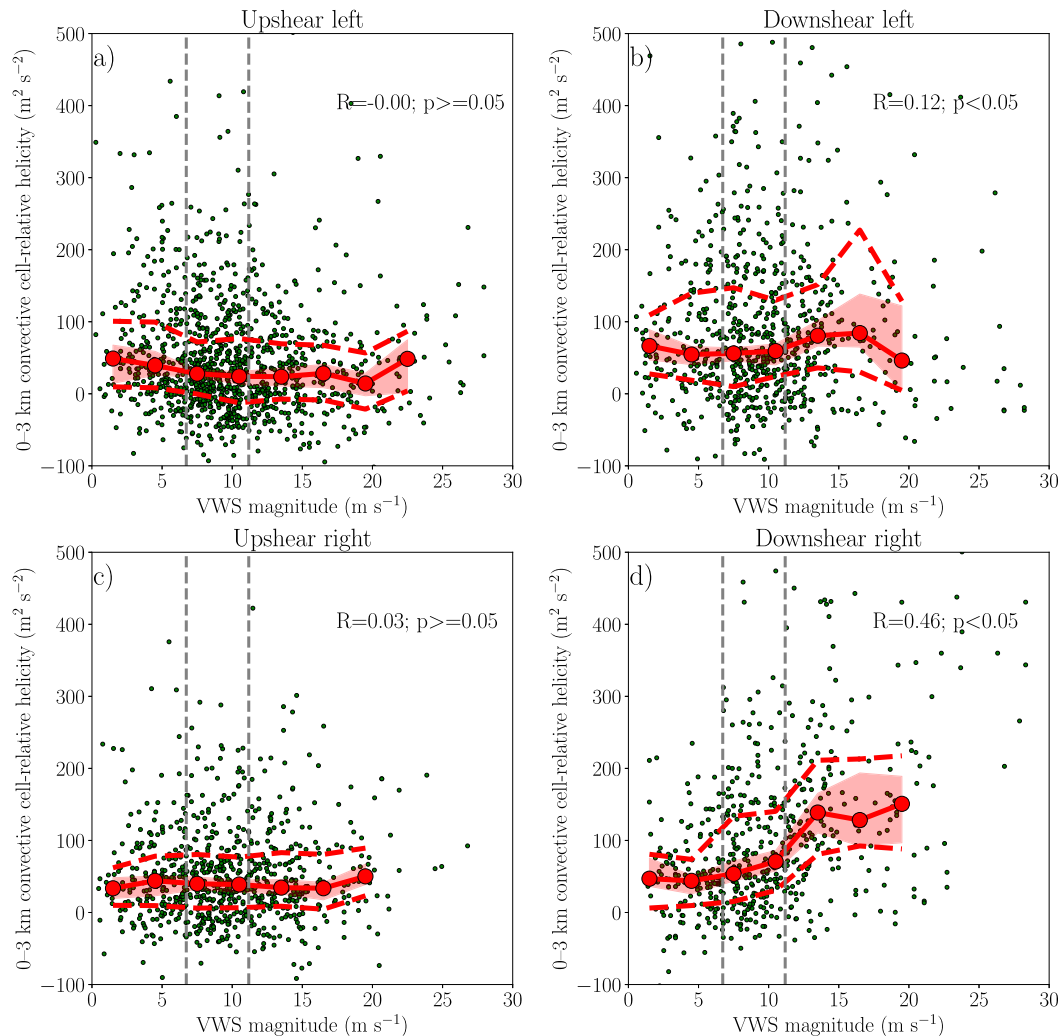


FIG. 10. Scatterplot (green dots) of VWS magnitude (m s^{-1} ; reanalysis derived) vs 0–3-km convective cell-relative helicity ($\text{m}^2 \text{s}^{-2}$; radiosonde derived) for all radiosondes within 500 km of the TC center in the (a) upshear left, (b) downshear left, (c) upshear right, and (d) downshear right. The red solid line, shading, and dashed red lines denote the median, its 95% confidence interval calculated using a 1000-sample bootstrap approach, and the interquartile range of helicity separated into 3 m s^{-1} VWS bins, respectively. Pearson correlation coefficients and p values are calculated using a 1000-sample bootstrap approach.

radial (Figs. 13a,c,e) and tangential (Figs. 13b,d,f) winds to examine the role of the VWS-induced enhancement of the TC primary and secondary circulation downshear in creating favorable kinematic environments (Molinari and Vollaro 2008, 2010). Our focus will be centered on the downshear-right quadrant, given the marginal changes in the tangential and radial winds for the three other VWS-related quadrants as VWS strengthens. In terms of convective cell-relative helicity sources, the vertical shear of the tangential wind term is generally dominant within 500 m of the surface, while the vertical shear of the radial wind term is generally dominant above this layer (Molinari and Vollaro 2008, 2010). Both

the radial and tangential wind in the downshear-right quadrant approximately double in magnitude throughout the lower troposphere between weak and strong VWS regimes, which is statistically different at the 95% confidence interval (Reasor et al. 2013; DeHart et al. 2014; Rogers et al. 2016; Nguyen et al. 2017). These differences are not associated with statistical changes in either TC intensity, outer size, or distance of the radiosonde from the TC center among the radiosondes in each VWS regime.

Next, we show that the ambient winds, by themselves, are not a dominant source of kinematically favorable environments for tornadic supercells. Specifically, composite median hodographs of the ambient winds

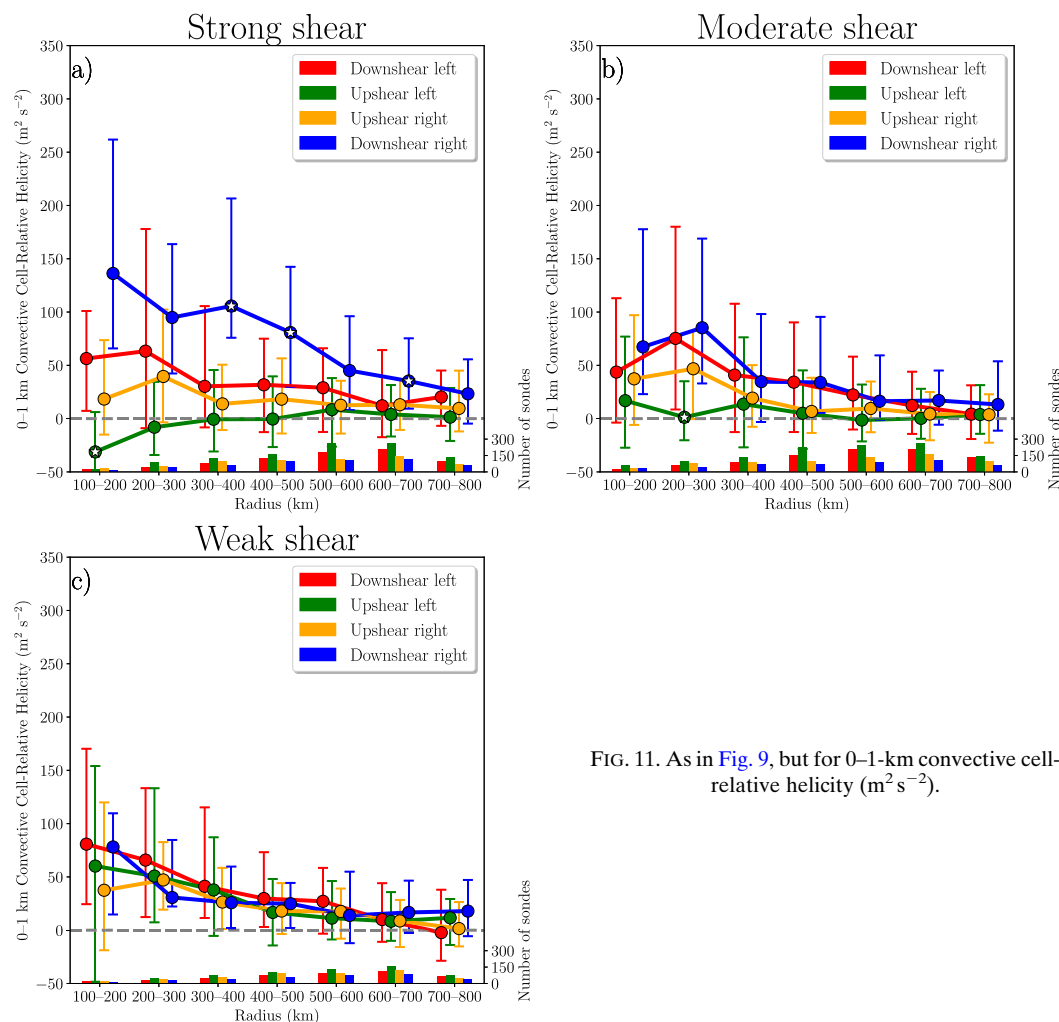


FIG. 11. As in Fig. 9, but for 0–1-km convective cell-relative helicity ($\text{m}^2 \text{s}^{-2}$).

(i.e., TC removed), from reanalysis data, are shown at the time of each radiosonde in Fig. 14. All three VWS regimes are characterized by weak changes in the speed and, to a lesser extent, angle of the ambient winds in the lower to midtroposphere, similar to prior work (Nolan 2011; Onderlinde and Nolan 2014; Finocchio and Majumdar 2017; Rios-Berrios and Torn 2017). In particular, 0–6-km vertical wind shear is greatest in strongly sheared TCs with values of 4.9 m s^{-1} , with much of the veering confined to the lower to midtroposphere. As an example, the 0–3-km convective cell-relative helicities for these hodographs are 26, 16, and $13 \text{ m}^2 \text{s}^{-2}$ for strong, moderate, and weakly sheared TCs, respectively. These values are typically associated with nonsupercellular convection (Rasmussen and Blanchard 1998; Thompson et al. 2003; Houston and Wilhelmson 2007). This marginal ambient lower-tropospheric helicity further suggests that the ambient winds by themselves cannot explain the increasing convective-scale helicity with

stronger VWS. Instead, the largest differences between VWS regimes are concentrated above 6 km, which is typically at or above the height of TC miniature supercells (Spratt et al. 1997; Suzuki et al. 2000; Baker et al. 2009; Eastin and Link 2009). However, the influence of vertical wind shear above 6 km on tornadic supercells, and particularly miniature supercells, has been understudied compared to below 6 km (Rasmussen and Straka 1998; Warren et al. 2017).

Despite the ambient winds being associated with marginal helicity, constructive superposition of the ambient winds with the TC winds is a key factor in creating favorable kinematic environments, particularly in the downshear-right quadrant. Figure 15 shows plan view plots of composite median ambient and TC wind vectors, and bar plots of median 0–3-km convective cell-relative helicity for the TC, ambient, and total winds. The helicity of the total winds (red bars) will exceed the sum of the TC (blue bars) and ambient winds (black

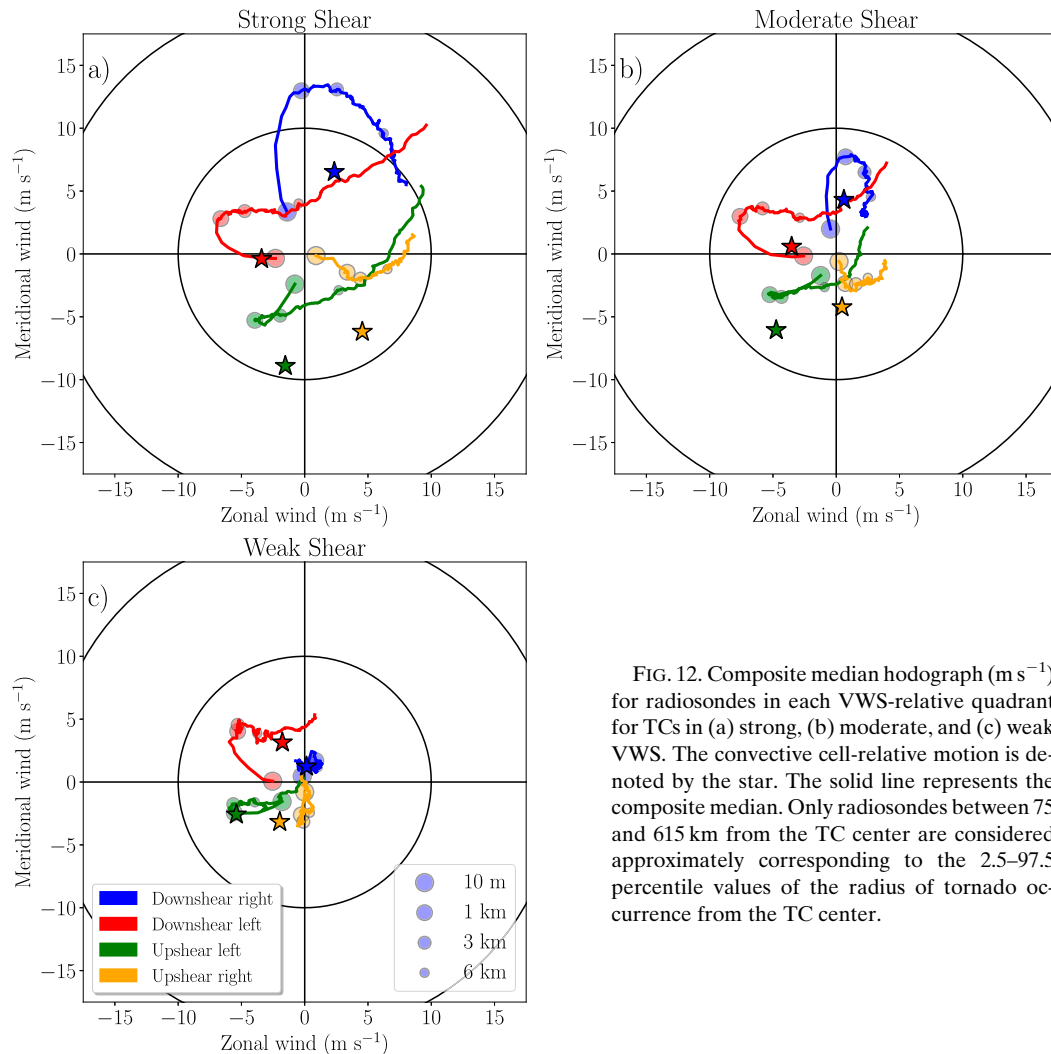


FIG. 12. Composite median hodograph (m s^{-1}) for radiosondes in each VWS-relative quadrant for TCs in (a) strong, (b) moderate, and (c) weak VWS. The convective cell-relative motion is denoted by the star. The solid line represents the composite median. Only radiosondes between 75 and 615 km from the TC center are considered approximately corresponding to the 2.5–97.5 percentile values of the radius of tornado occurrence from the TC center.

bars) when the TC and ambient winds are strongly in phase (and vice versa) since helicity is the nonlinear product of the wind field. Consistent with Fig. 2, the TC and ambient wind vectors are most strongly in phase in the downshear-right quadrant. Moreover, the TC winds in the downshear-right quadrant increase as VWS strengthens partially in association with the VWS-induced enhancement of the TC secondary circulation. However, the weaker winds in weakly sheared TCs are also partially an artifact of the large variability in the VWS vector direction and, hence, which TC sectors (e.g., northeast sector) are downshear yielding cancellation between TC winds when composited over a large number of cases. While the increases in ambient and TC winds are both associated with enhanced helicity in the downshear-right quadrant, their combined contribution nonlinearly enhances the median helicity of the total wind field to be: 1) 50% larger than the median helicity

associated with the TC wind field and 2) 25% larger than the helicity of the TC and ambient winds calculated separately and then added together. Both of these differences are statistically different at the 95% confidence interval. In contrast, the ambient and TC winds in the upshear-left quadrant are strongly out of phase such that the helicity of the total wind field is statistically smaller at the 95% confidence interval than the helicity from the TC and ambient wind calculated separately, and then summed together. Last, the ambient and TC winds in the two remaining quadrants are sufficiently out of phase such that there is not a nonlinear enhancement of the helicity associated with the total wind field beyond the sum of TC and ambient wind components.

Together, these results suggest that the downshear-right quadrant in strongly sheared TCs is most frequently kinematically favorable for tornadoes potentially in association with four factors:

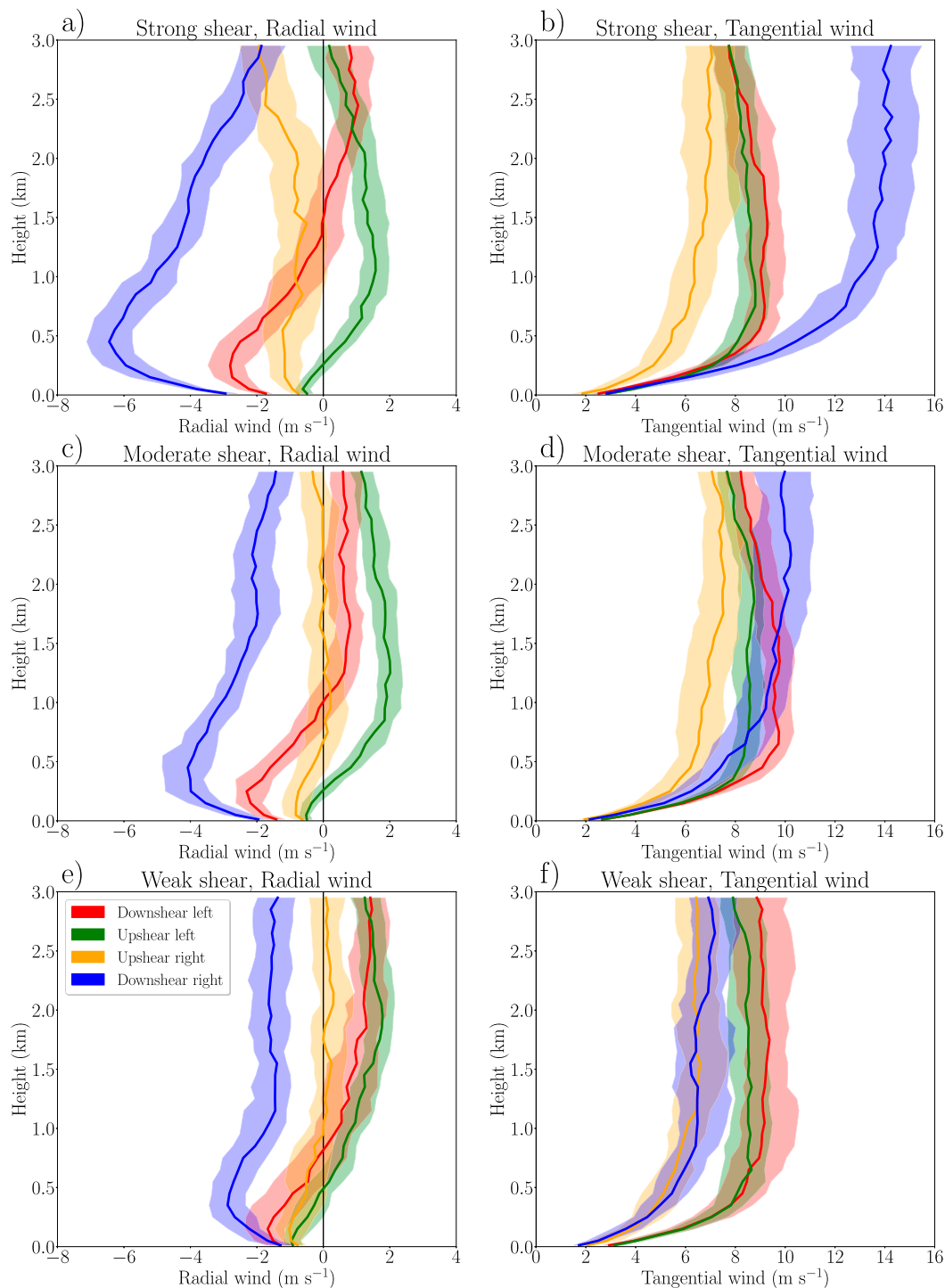


FIG. 13. Composite median (solid line) and its 95% confidence interval (shading) of vertical profiles of cyclone-relative radial wind (m s^{-1}) and tangential wind (m s^{-1}) computed from radiosondes in each of the VWS-relative quadrants for TCs in (a),(b) strong; (c),(d) moderate; and (e),(f) weak VWS. Only radiosondes between 75 and 615 km from the TC center are considered approximately corresponding to the 2.5–97.5 percentile values of the radius of tornado occurrence from the TC center.

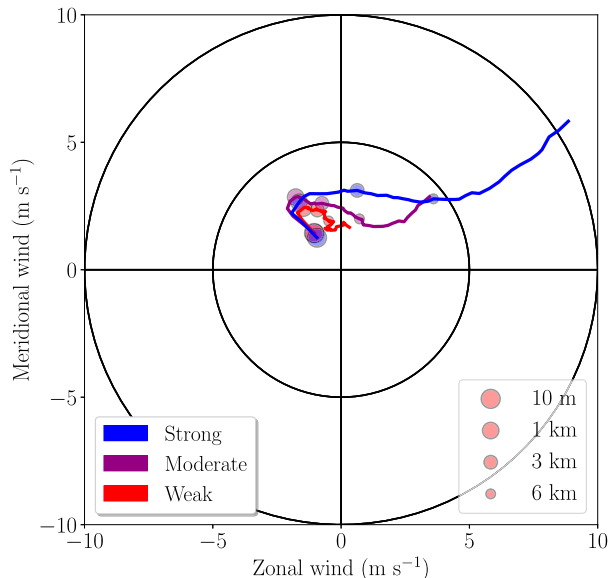


FIG. 14. Composite median hodographs of ambient winds from the ERA5 reanalysis at the time of the radiosonde with the TC circulation removed following Davis et al. (2008) for TCs in strong, moderate, and weak VWS. Radiosondes in each VWS category are aggregated together from all VWS-relative quadrants.

- Constructive superposition of the TC and ambient winds, which nonlinearly contributes to enhanced helicity (Molinari and Vollaro 2008, 2010; Gu et al. 2018);
- Enhanced TC secondary and primary circulation downshear in response to VWS (Franklin et al. 1993; Black et al. 2002; Molinari and Vollaro 2008, 2010);
- Generation of a lower to midtropospheric tangential jet in the TC rainbands due to vertical momentum transport by enhanced deep convection, especially in strongly sheared TCs (i.e., feedback of VWS-induced convective enhancement; May and Holland 1999; Hense and Houze 2008; Didlake and Houze 2013; Hense and Houze 2012);
- The development of warm conveyor belts (i.e., southerly jet) that occur during extratropical transition (Klein et al. 2000; Ritchie and Elsberry 2001; Jones et al. 2003);

Of these factors, the fourth hypothesis may be least relevant since only 13% of TCs are undergoing extratropical transition at landfall in the Atlantic (Bieli et al. 2019). However, additional work is necessary before any single factor can be ruled out. Moreover, further investigation is needed to identify whether favorable environments exist in association with the inner-core, downshear-left tornado maximum, which cannot be investigated by radiosondes near the TC center.

d. Thermodynamic environments

Distributions of 0–3-km CAPE show increasing differences among the VWS-relative quadrants as VWS

strengthens (Fig. 16). Regardless of the VWS regime, 0–3-km CAPE falls within the range typically associated with tornadic supercells at all radii in each quadrant (i.e., $18\text{--}92\text{ J kg}^{-1}$; Rasmussen 2003). However, the downshear right generally has the greatest CAPE and is the only quadrant with median values at all TC radii in all three VWS regimes that consistently exceed this range. In contrast, the left-of-VWS vector quadrants show that CAPE substantially decreases with increasing VWS. Specifically, median CAPE in these two quadrants is 28%–68% smaller, and statistically different at the 95% confidence interval, in strongly sheared TCs compared to weakly sheared cases. Last, CAPE in the upshear-right quadrant shows no statistical changes with increasing VWS. As a result, the downshear-right quadrant of strongly sheared TCs has statistically larger 0–3-km CAPE, at the 95% confidence interval, than the other three quadrants for TC radii between 200 and 700 km (Molinari et al. 2012). In contrast, there are no interquadrant statistical differences in weakly or moderately sheared TCs.

The nonlinear dependence of 0–3-km CAPE upon VWS is shown in Fig. 17. The quadrants to the left of the VWS vector show large decreases in CAPE with increasing VWS, whereas the right-of-VWS-quadrants show no statistical changes. In particular, the median CAPE in the upshear and downshear left decreases by 54% and 72%, respectively. The response of CAPE to VWS in each quadrant is also strongly nonlinear, with weak Pearson correlation coefficients ($-0.25 \leq R \leq 0.14$).

Composite median skew T –log p diagrams show the full vertical structure of moisture and temperature in TCs within each of the three VWS regimes (Fig. 18). Compared to weakly sheared TCs, the downshear-right quadrant of strongly sheared cases is characterized by the following statistical differences (at the 95% confidence interval) that may be due to enhanced convection: 1) lower-tropospheric cooling, maximized above the surface, with changes in median values ranging between -0.4° and -0.9°C , 2) warming of the upper troposphere with median values ranging between 0.4° and 0.9°C , and 3) moistening of the troposphere, particularly the upper troposphere, with differences in median values upward of 7.6°C . Together, these differences are associated with marginal changes in 0–3-km CAPE as VWS increases (Fig. 16). In contrast, the remaining three quadrants show either drying or marginal changes in lower-tropospheric moisture as VWS increases, while exhibiting lower-tropospheric cooling similar in magnitude to the downshear-right quadrant in association with reduced 0–3-km CAPE.

In addition to this lower-tropospheric cooling, the upshear-left and downshear-left quadrants more broadly

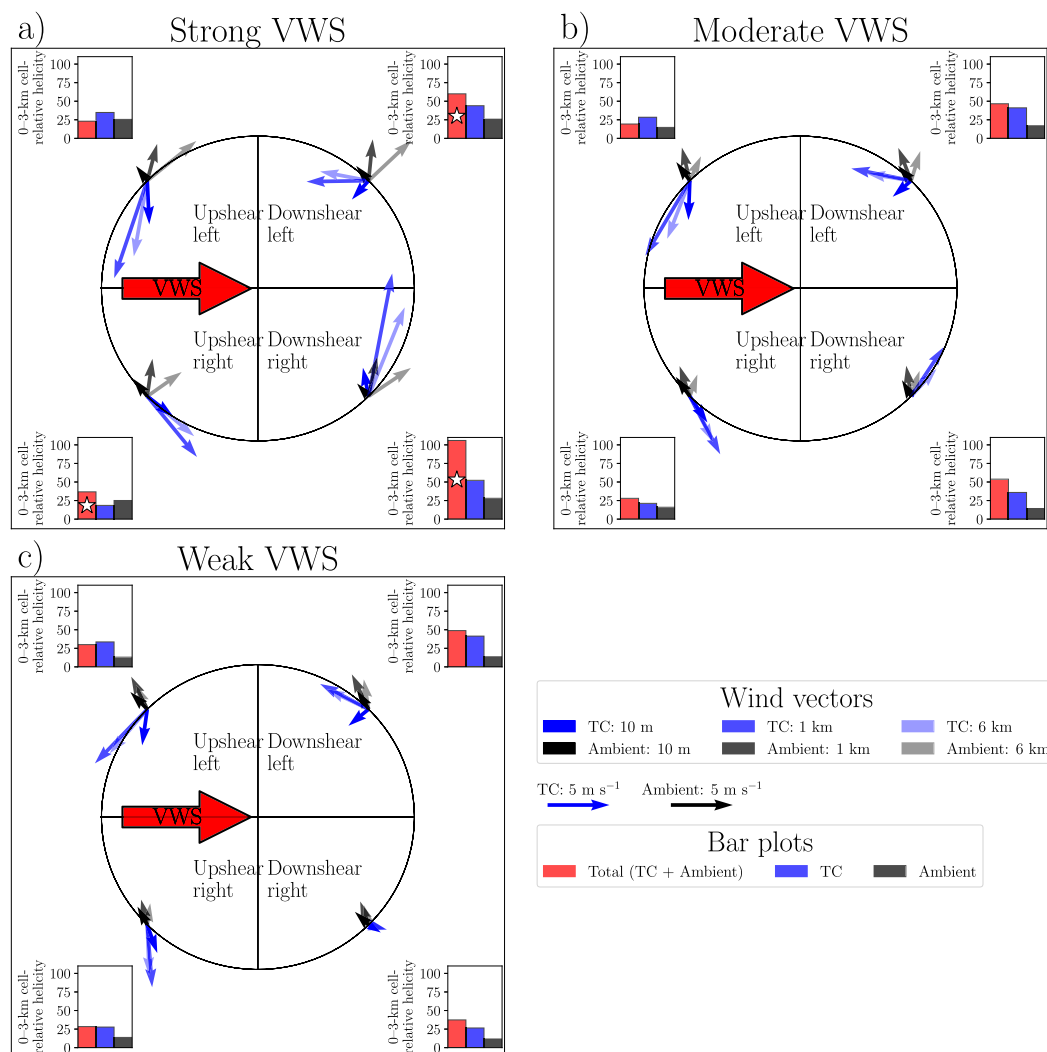


FIG. 15. Plan view plot of composite median 10-m, 1-km, and 6-km wind vectors (m s^{-1}) for the TC and ambient wind field, and bar plots of composite median 3-km convective cell-relative helicity ($\text{m}^2 \text{s}^{-2}$) for the total (i.e., TC wind and ambient wind), TC, and ambient wind field in each VWS-relative quadrant within (a) strongly, (b) moderately, and (c) weakly sheared TCs. The white stars denote quadrants in which the median helicity associated with the total wind field is statistically greater than that associated with the TC wind field at the 95% confidence interval. The radiosonde data have been coarsened to the vertical grid spacing of the reanalysis data for these calculations.

show cooling in the mid- to upper troposphere as VWS increases with differences in median values between -0.7° and -2.2°C , which are statistically different at the 95% confidence interval. However, this mid- and upper-tropospheric cooling is weaker than in the lower troposphere promoting thermodynamic stabilization of the column. The mid- and upper troposphere in the upshear-left and, to a lesser extent, the upshear-right quadrant also shows stronger dry anomalies with stronger VWS compared to the downshear quadrants, with peak differences in median dewpoint values of 10.0°C . These differences are statistically

different at the 95% confidence interval. This mid-tropospheric drying in the upshear quadrants, which are typically left-of-motion, is similar to prior work (McCaul 1987, 1991; Curtis 2004).

These CAPE asymmetries with increasing VWS may be attributed to six different factors:

- VWS-induced subsidence from the TC secondary circulation on the upshear half of the TC yielding tropospheric drying (Jones 1995; Frank and Ritchie 1999; Black et al. 2002);
- Enhanced convection in more strongly sheared TCs generates stronger downdrafts (especially when

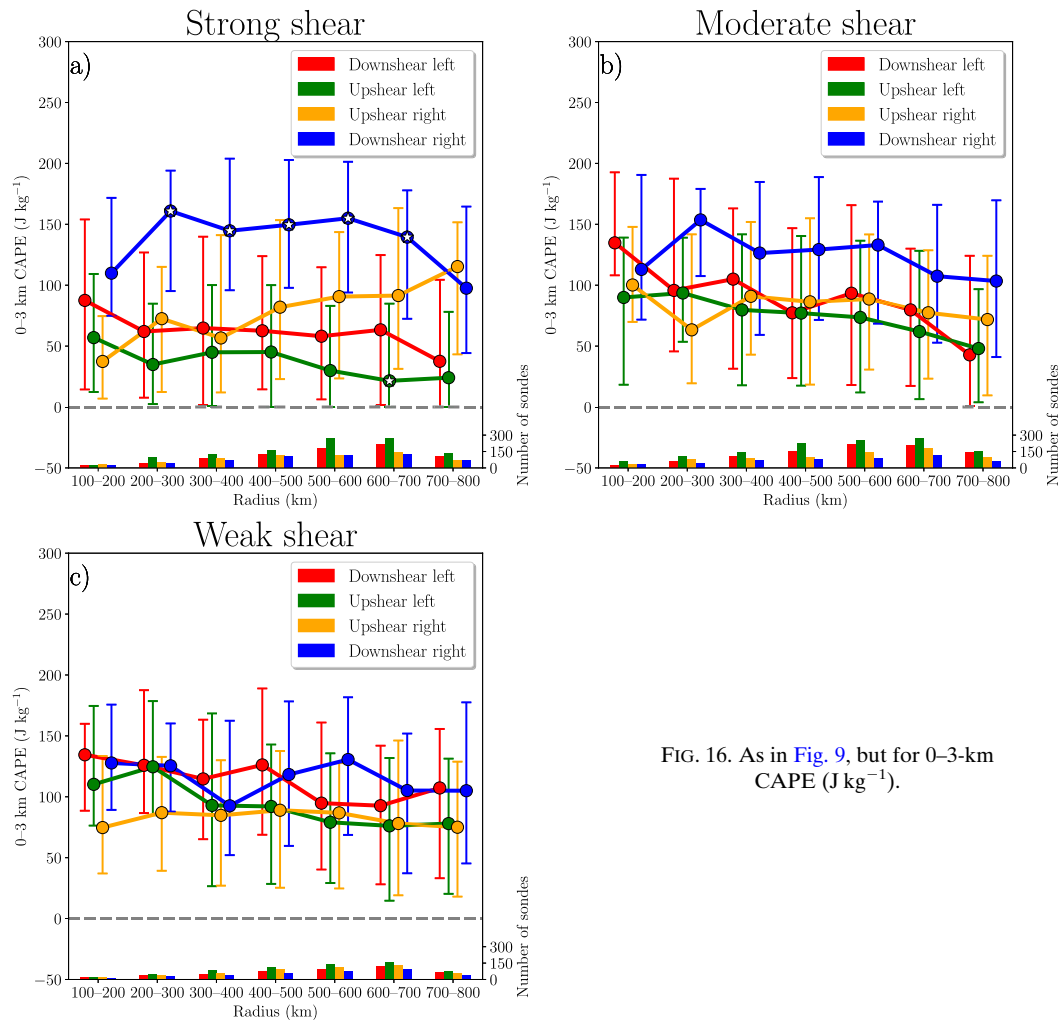


FIG. 16. As in Fig. 9, but for 0–3-km CAPE (J kg^{-1}).

entraining dry, midtropospheric air) that are cyclonically advected into the downshear-left, upshear-left, and upshear-right quadrant (Riemer et al. 2010; Tang and Emanuel 2010, 2012; Zhang et al. 2013) yielding lower-tropospheric cooling, while causing tropospheric moistening, and upper-tropospheric warming downshear right;

- The downshear-right quadrant is often the southeast quadrant (Fig. 6b), which typically has direct access to warm, moist onshore flow explaining the marginal CAPE changes as VWS increases;
- Downshear advection of upper-tropospheric anvil clouds by the upper-tropospheric winds associated with strong VWS may reduce surface radiative heating in the downshear quadrants;
- Dry, subsiding air in strongly sheared TCs may be triggered by evaporative cooling as light stratiform precipitation falls into unsaturated air beneath anvil clouds before being advected cyclonically into the

upshear quadrants (Dolling and Barnes 2012; Kerns and Chen 2015; Nguyen et al. 2017);

- Increasing VWS is associated with stronger baroclinic zones, especially during extratropical transition, yielding a reduction in 0–3-km CAPE due to the entrainment of cooler, drier ambient air into the left-of-shear quadrants, with eventual cyclonic advection into the upshear-right quadrant (Fig. 2h; Jones 1995; Ritchie and Elsberry 2001; Nguyen et al. 2017).

Each of these factors could play a role in generating the temperature and moisture anomalies documented here (Zawislak et al. 2016; Nguyen et al. 2017, 2019). However, identifying which of these factors is most important is beyond the scope of the observations analyzed here, and instead requires a systematic modeling assessment.

These results together with the kinematic analysis suggest that the downshear-right quadrant of strongly

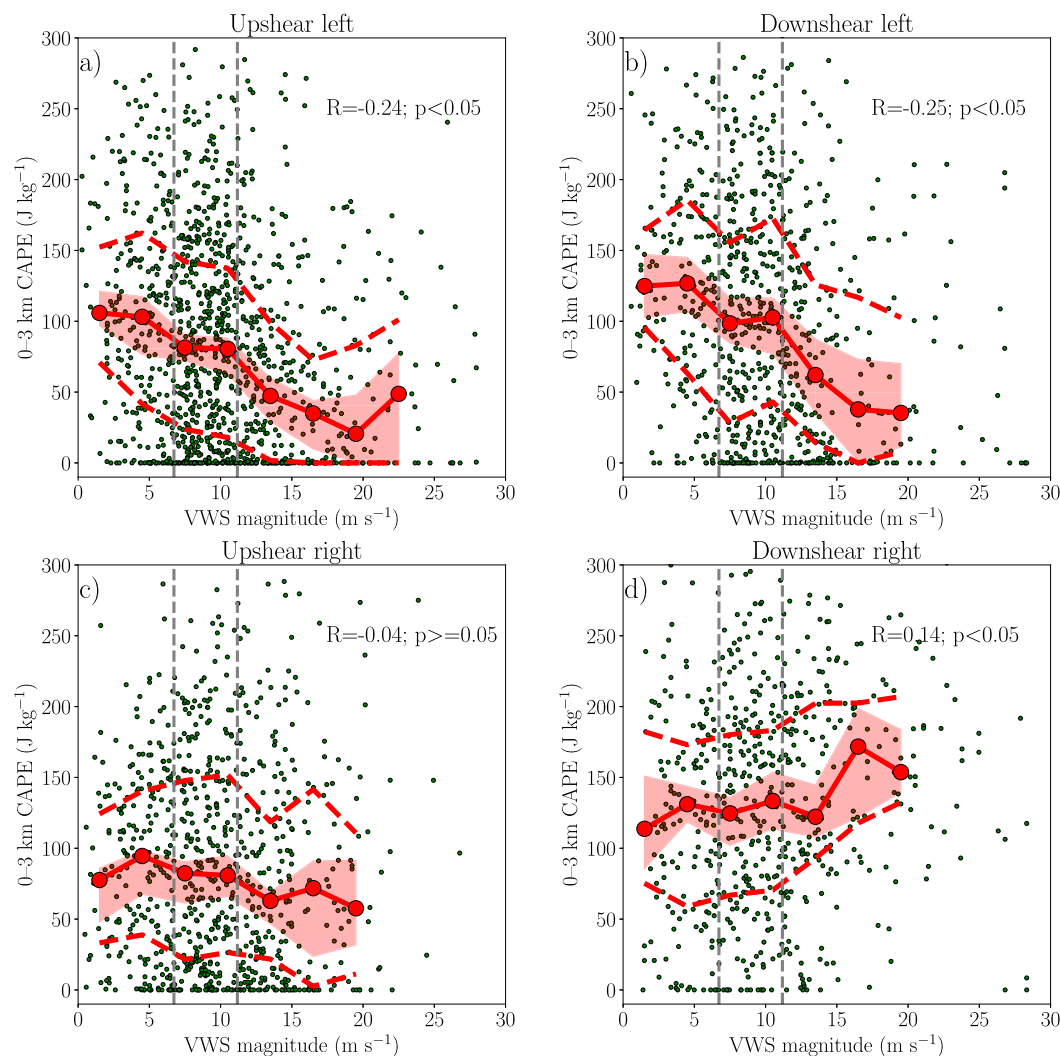


FIG. 17. As in Fig. 10, but for VWS magnitude (m s^{-1}) vs 0–3-km CAPE (J kg^{-1}).

sheared TCs is most frequently associated with favorable tornadic environments. In contrast, the limiting factor for tornadoes in the remaining three VWS-relative quadrants is the kinematic environment. These patterns in the kinematic and thermodynamic environments and tornado occurrence seem most consistent with both the: 1) constructive superposition of ambient and TC winds and the 2) VWS-induced enhancement of the TC secondary circulation. However, further work is necessary before ruling out any particular process.

4. Summary and discussion

The goal of the present study was to investigate the impact of VWS upon tornado frequency, location, and their associated environments in TCs. Specifically, we first defined weak, moderate, and strong VWS

thresholds based upon the terciles of the reanalysis-derived VWS distribution for all Atlantic TCs. Using observed tornado reports in TCs from 1995 to 2018, tornado frequency and cyclone-relative location were analyzed for each VWS category. To provide a physical basis for these results, radiosonde data were binned according to the VWS magnitude and VWS-relative quadrant to diagnose the kinematic and thermodynamic environmental sensitivity to VWS.

Our results showed that VWS appeared to influence both the frequency and cyclone-relative location of tornadoes in TCs. Specifically, the majority of tornadoes, especially EF1+/F1+ tornadoes, occur in strongly sheared TCs. This result is attributable to enhanced rates of tornado production per 6-h period, especially for higher-end tornado production, in stronger, more southwesterly VWS. However, too strong of VWS may

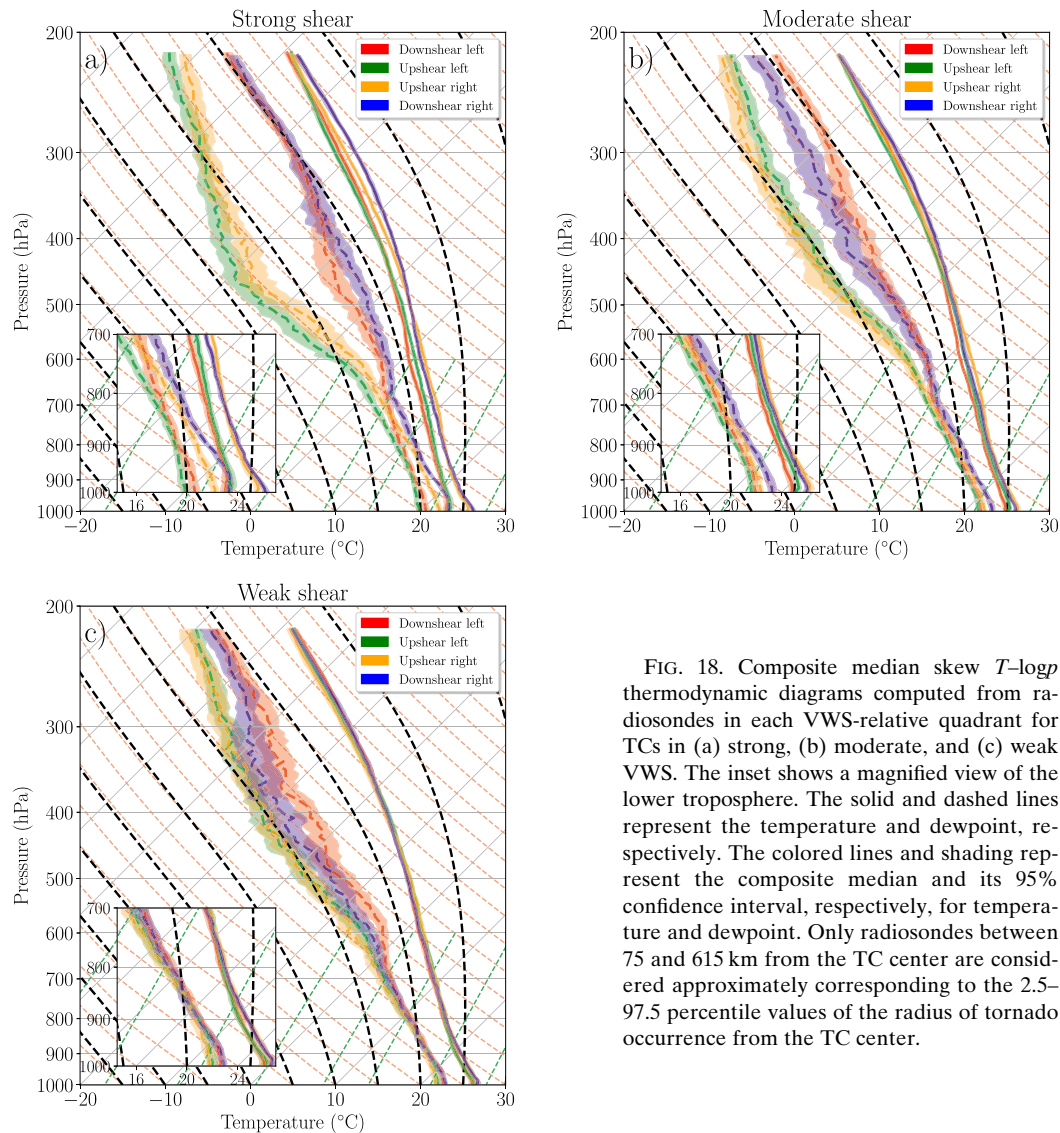


FIG. 18. Composite median skew T -log p thermodynamic diagrams computed from radiosondes in each VWS-relative quadrant for TCs in (a) strong, (b) moderate, and (c) weak VWS. The inset shows a magnified view of the lower troposphere. The solid and dashed lines represent the temperature and dewpoint, respectively. The colored lines and shading represent the composite median and its 95% confidence interval, respectively, for temperature and dewpoint. Only radiosondes between 75 and 615 km from the TC center are considered approximately corresponding to the 2.5–97.5 percentile values of the radius of tornado occurrence from the TC center.

favor TC weakening and disruption of both its convective structure and tornado production. Stronger VWS is associated with tornadoes that are increasingly confined to the downshear half of the TC. Tornado location also changed with increasing radius in strongly sheared TCs, such that their location gradually transitioned from the downshear-left quadrant near the TC center to the downshear-right quadrant in the TC outer region.

Radiosonde data showed that the downshear-right quadrant of strongly sheared TCs is most frequently associated with favorable kinematic environments for tornadoes. Specifically, 0–3- and 0–1-km convective cell-relative helicity in the downshear-right quadrant of strongly sheared TCs, within 500 km of the TC center, often exceeded previously defined empirical values associated with tornadic supercells.

This enhanced helicity was possibly associated with strong near-surface speed shear and veering above this layer due to the constructive superposition of the ambient and TC winds, and the VWS-induced enhancement of the TC secondary and primary wind field downshear.

Analysis of radiosondes showed that thermodynamic environments are favorable for tornadic supercells in all quadrants regardless of VWS. However, the downshear-right quadrant in TCs typically has the largest 0–3-km CAPE in all VWS regimes that is well above the range associated with tornadic supercells. Similarly, 0–3-km CAPE in the upshear-right quadrant remains unchanged with stronger VWS. In contrast, the left-of-shear VWS-relative quadrants show decreased 0–3-km CAPE at most radii as VWS increases, although CAPE remains

favorable for tornadic supercells. Additional work is needed to identify which of the many potential physical processes are responsible for these VWS-relative asymmetries in thermodynamic environments for tornadoes in TCs.

In summary, these results suggest that strong VWS is a key factor in enhancing TC tornado production, with the most favorable kinematic environments located within the downshear-right quadrant. Strong VWS also causes tornadoes to most often occur in the northeastern quadrant of the TC, while variations in VWS among cases may help explain the large variability in tornado production among TCs. VWS may potentially create favorable kinematic environments for tornadoes due to a combination of vector superposition between the ambient and TC winds, and the VWS-induced enhancement of the TC circulation in the downshear half of the TC. However, additional work is necessary to definitively isolate the physical processes whereby VWS creates favorable environments for tornadoes and why inner-core tornadoes preferentially occur in the downshear-left quadrant. The results presented here are especially useful since the prediction of TC tornadoes are typically less skillful at all lead times compared to their non-TC counterparts (Edwards 2012; Martinaitis 2017). More broadly, these results also better inform our understanding of the sensitivity of deep convection in TCs and their associated hazards (e.g., flooding) to VWS. While extreme convective rainfall in landfalling and inland TCs is outside the scope of our work, our results with tornadic convection indicate potential operational utility for analogous, VWS-relative environmental analyses aimed at quantitative precipitation forecasting (QPF). This study also motivates analysis comparing how the relationship between tornadoes in TCs and VWS may vary when controlling for other previously identified factors (e.g., diurnal cycle).

Acknowledgments. This study is generously supported by the Cooperative Institute for Mesoscale Meteorological Studies (CIMMS) and the University of Oklahoma. The statements, findings, conclusions, and recommendations herein are those of the authors and do not necessarily reflect the views of the University of Oklahoma, CIMMS, and NOAA. The authors thank Christopher Nowotarski (TAMU), two anonymous reviewers, and Elizabeth Ritchie (UNSW) for their constructive comments. The authors would also like to thank Nusrat Yussouf (NSSL/OU), Eugene McCaul Jr. (USRA), Lou Wicker (NSSL), Morris Weisman (NCAR), George Bryan (NCAR), Stan Trier (NCAR), John Knaff (CIRA), Anthony Didlake (Penn State), Ellie Casas (CSU), Chris Davis (NCAR), Greg McFarquhar (OU/CIMMS), Matthew Bunkers (NOAA/NWS), and Robert Hart

(FSU) for insightful suggestions. This work would not have been possible without the availability of TCTOR data from NOAA SPC, the ERA5 reanalysis from the ECMWF, and the NCAR Research and Data Archive, IBTrACS data from NOAA/NCDC, and the IGRA radiosonde data from NOAA. All figures were made using Matplotlib (Hunter 2007) and MetPy (May et al. 2020). All kinematic and thermodynamic parameters were computed using SHARPPy (Blumberg et al. 2017).

REFERENCES

- Abarca, S. F., K. L. Corbosiero, and D. Vollaro, 2011: The World Wide Lightning Location Network and convective activity in tropical cyclones. *Mon. Wea. Rev.*, **139**, 175–191, <https://doi.org/10.1175/2010MWR3383.1>.
- Baker, A. K., M. D. Parker, and M. D. Eastin, 2009: Environmental ingredients for supercells and tornadoes within Hurricane Ivan. *Wea. Forecasting*, **24**, 223–244, <https://doi.org/10.1175/2008WAF2222146.1>.
- Bender, M., 1997: The effect of relative flow on the asymmetric structure in the interior of hurricanes. *J. Atmos. Sci.*, **54**, 703–724, [https://doi.org/10.1175/1520-0469\(1997\)054<0703:TEORFO>2.0.CO;2](https://doi.org/10.1175/1520-0469(1997)054<0703:TEORFO>2.0.CO;2).
- Bieli, M., S. J. Camargo, A. H. Sobel, J. L. Evans, and T. Hall, 2019: A global climatology of extratropical transition. Part I: Characteristics across basins. *J. Climate*, **32**, 3557–3582, <https://doi.org/10.1175/JCLI-D-17-0518.1>.
- Black, M., J. Gamache, F. Marks, C. Samsury, and H. Willoughby, 2002: Eastern Pacific Hurricanes Jimena of 1991 and Olivia of 1994: The effect of vertical shear on structure and intensity. *Mon. Wea. Rev.*, **130**, 2291–2312, [https://doi.org/10.1175/1520-0493\(2002\)130<2291:EPHJOA>2.0.CO;2](https://doi.org/10.1175/1520-0493(2002)130<2291:EPHJOA>2.0.CO;2).
- Blake, E., and D. Zelinsky, 2018: Tropical cyclone report: Hurricane Harvey (17 August–1 September 2017), NHC Tech. Rep. AL092017, 77 pp., https://www.nhc.noaa.gov/data/tcr/AL092017_Harvey.pdf.
- Blumberg, W. G., K. T. Halbert, T. A. Supinie, P. T. Marsh, R. L. Thompson, and J. A. Hart, 2017: SHARPPy: An open-source sounding analysis toolkit for the atmospheric sciences. *Bull. Amer. Meteor. Soc.*, **98**, 1625–1636, <https://doi.org/10.1175/BAMS-D-15-00309.1>.
- Bosart, L. F., and D. B. Dean, 1991: The Agnes rainstorm of June 1972: Surface feature evolution culminating in inland storm redevelopment. *Wea. Forecasting*, **6**, 515–537, [https://doi.org/10.1175/1520-0434\(1991\)006<0515:TAROJS>2.0.CO;2](https://doi.org/10.1175/1520-0434(1991)006<0515:TAROJS>2.0.CO;2).
- Brown, R. A., D. W. Burgess, and K. C. Crawford, 1973: Twin tornado cyclones within a severe thunderstorm: Single Doppler radar observations. *Weatherwise*, **26**, 63–71, <https://doi.org/10.1080/00431672.1973.9931634>.
- Bunkers, M. J., B. A. Klimowski, J. W. Zeitler, R. L. Thompson, and M. L. Weisman, 2000: Predicting supercell motion using a new hodograph technique. *Wea. Forecasting*, **15**, 61–79, [https://doi.org/10.1175/1520-0434\(2000\)015<0061:PSMUAN>2.0.CO;2](https://doi.org/10.1175/1520-0434(2000)015<0061:PSMUAN>2.0.CO;2).
- Chavas, D., and K. Emanuel, 2010: A QuikSCAT climatology of tropical cyclone size. *Geophys. Res. Lett.*, **37**, L18816, <https://doi.org/10.1029/2010GL044558>.
- , N. Lin, W. Dong, and Y. Lin, 2016: Observed tropical cyclone size revisited. *J. Climate*, **29**, 2923–2939, <https://doi.org/10.1175/JCLI-D-15-0731.1>.
- Chen, S. S., J. A. Knaff, and F. D. Marks, 2006: Effects of vertical wind shear and storm motion on tropical cyclone rainfall

- asymmetries deduced from TRMM. *Mon. Wea. Rev.*, **134**, 3190–3208, <https://doi.org/10.1175/MWR3245.1>.
- Corbosiero, K., and J. Molinari, 2002: The effects of vertical wind shear on the distribution of convection in tropical cyclones. *Mon. Wea. Rev.*, **130**, 2110–2123, [https://doi.org/10.1175/1520-0493\(2002\)130<2110:TEOVWS>2.0.CO;2](https://doi.org/10.1175/1520-0493(2002)130<2110:TEOVWS>2.0.CO;2).
- , and —, 2003: The relationship between storm motion, vertical wind shear, and convective asymmetries in tropical cyclones. *J. Atmos. Sci.*, **60**, 366–376, [https://doi.org/10.1175/1520-0469\(2003\)060<0366:TRBSMV>2.0.CO;2](https://doi.org/10.1175/1520-0469(2003)060<0366:TRBSMV>2.0.CO;2).
- Curtis, L., 2004: Midlevel dry intrusions as a factor in tornado outbreaks associated with landfalling tropical cyclones from the Atlantic and Gulf of Mexico. *Wea. Forecasting*, **19**, 411–427, [https://doi.org/10.1175/1520-0434\(2004\)019<0411:MDIAAF>2.0.CO;2](https://doi.org/10.1175/1520-0434(2004)019<0411:MDIAAF>2.0.CO;2).
- Davies, J., 1990: Midget supercell spawns tornadoes. *Weatherwise*, **43**, 260, <https://doi.org/10.1080/00431672.1990.9929350>.
- Davies-Jones, R., 1984: Streamwise vorticity: The origin of updraft rotation in supercell storms. *J. Atmos. Sci.*, **41**, 2991–3006, [https://doi.org/10.1175/1520-0469\(1984\)041<2991:SVTOOU>2.0.CO;2](https://doi.org/10.1175/1520-0469(1984)041<2991:SVTOOU>2.0.CO;2).
- Davis, C., C. Snyder, and A. C. Didlake, 2008: A vortex-based perspective of eastern Pacific tropical cyclone formation. *Mon. Wea. Rev.*, **136**, 2461–2477, <https://doi.org/10.1175/2007MWR2317.1>.
- DeHart, J. C., R. A. Houze Jr., and R. F. Rogers, 2014: Quadrant distribution of tropical cyclone inner-core kinematics in relation to environmental shear. *J. Atmos. Sci.*, **71**, 2713–2732, <https://doi.org/10.1175/JAS-D-13-0298.1>.
- DeMaria, M., 1996: The effect of vertical shear on tropical cyclone intensity change. *J. Atmos. Sci.*, **53**, 2076–2088, [https://doi.org/10.1175/1520-0469\(1996\)053<2076:TEOVSO>2.0.CO;2](https://doi.org/10.1175/1520-0469(1996)053<2076:TEOVSO>2.0.CO;2).
- , and J. Kaplan, 1994: A Statistical Hurricane Intensity Prediction Scheme (SHIPS) for the Atlantic Basin. *Wea. Forecasting*, **9**, 209–220, [https://doi.org/10.1175/1520-0434\(1994\)009<0209:ASHIPS>2.0.CO;2](https://doi.org/10.1175/1520-0434(1994)009<0209:ASHIPS>2.0.CO;2).
- , M. Mainelli, L. K. Shay, J. A. Knaff, and J. Kaplan, 2005: Further improvements to the Statistical Hurricane Intensity Prediction Scheme (SHIPS). *Wea. Forecasting*, **20**, 531–543, <https://doi.org/10.1175/WAF862.1>.
- Didlake, A. C., and R. A. Houze, 2013: Convective-scale variations in the inner-core rainbands of a tropical cyclone. *J. Atmos. Sci.*, **70**, 504–523, <https://doi.org/10.1175/JAS-D-12-0134.1>.
- Ditchek, S. D., J. Molinari, K. L. Corbosiero, and R. G. Fovell, 2019: An objective climatology of tropical cyclone diurnal pulses in the Atlantic basin. *Mon. Wea. Rev.*, **147**, 591–605, <https://doi.org/10.1175/MWR-D-18-0368.1>.
- Dolling, K., and G. M. Barnes, 2012: Warm-core formation in tropical storm Humberto (2001). *Mon. Wea. Rev.*, **140**, 1177–1190, <https://doi.org/10.1175/MWR-D-11-00183.1>.
- Droegemeier, K. K., S. M. Lazarus, and R. Davies-Jones, 1993: The influence of helicity on numerically simulated convective storms. *Mon. Wea. Rev.*, **121**, 2005–2029, [https://doi.org/10.1175/1520-0493\(1993\)121<2005:TIOHON>2.0.CO;2](https://doi.org/10.1175/1520-0493(1993)121<2005:TIOHON>2.0.CO;2).
- Durre, I., R. S. Vose, and D. B. Wuertz, 2006: Overview of the integrated global radiosonde archive. *J. Climate*, **19**, 53–68, <https://doi.org/10.1175/JCLI3594.1>.
- Eastin, M. D., and M. C. Link, 2009: Miniature supercells in an offshore outer rainband of Hurricane Ivan (2004). *Mon. Wea. Rev.*, **137**, 2081–2104, <https://doi.org/10.1175/2009MWR2753.1>.
- Edwards, R., 2010: Tropical cyclone tornado records for the modernized National Weather Service era. *25th Conf. on Severe Local Storms*, Denver, CO, Amer. Meteor. Soc., P3.1, https://ams.confex.com/ams/25SLS/techprogram/paper_175269.htm.
- , 2012: Tropical cyclone tornadoes: A review of knowledge in research and prediction. *Electron. J. Severe Storms Meteor.*, **7** (6), <http://www.ejssm.org/ojs/index.php/ejssm/article/view/97/84>.
- , and R. Thompson, 2012: Reversible CAPE in tropical cyclone tornado regimes. *27th Conf. on Severe Local Storms*, Madison, WI, Amer. Meteor. Soc., 88, <https://ams.confex.com/ams/27SLS/webprogram/Paper254328.html>.
- , A. R. Dean, R. L. Thompson, and B. T. Smith, 2012: Convective modes for significant severe thunderstorms in the contiguous United States. Part III: Tropical cyclone tornadoes. *Wea. Forecasting*, **27**, 1507–1519, <https://doi.org/10.1175/WAF-D-11-00117.1>.
- Emanuel, K., 1986: An air-sea interaction theory for tropical cyclones. Part I: Steady-state maintenance. *J. Atmos. Sci.*, **43**, 585–605, [https://doi.org/10.1175/1520-0469\(1986\)043<0585:AASITF>2.0.CO;2](https://doi.org/10.1175/1520-0469(1986)043<0585:AASITF>2.0.CO;2).
- Finocchio, P. M., and S. J. Majumdar, 2017: A statistical perspective on wind profiles and vertical wind shear in tropical cyclone environments of the Northern Hemisphere. *Mon. Wea. Rev.*, **145**, 361–378, <https://doi.org/10.1175/MWR-D-16-0221.1>.
- Frank, W. M., 1977: The structure and energetics of the tropical cyclone. Part I: Storm structure. *Mon. Wea. Rev.*, **105**, 1119–1135, [https://doi.org/10.1175/1520-0493\(1977\)105<1119:TSAEOT>2.0.CO;2](https://doi.org/10.1175/1520-0493(1977)105<1119:TSAEOT>2.0.CO;2).
- , 1982: Large-scale characteristics of tropical cyclones. *Mon. Wea. Rev.*, **110**, 572–586, [https://doi.org/10.1175/1520-0493\(1982\)110<0572:LSCOTC>2.0.CO;2](https://doi.org/10.1175/1520-0493(1982)110<0572:LSCOTC>2.0.CO;2).
- , and E. A. Ritchie, 1999: Effects of environmental flow upon tropical cyclone structure. *Mon. Wea. Rev.*, **127**, 2044–2061, [https://doi.org/10.1175/1520-0493\(1999\)127<2044:EOEFUT>2.0.CO;2](https://doi.org/10.1175/1520-0493(1999)127<2044:EOEFUT>2.0.CO;2).
- Franklin, J. L., S. J. Lord, S. E. Feuer, and F. D. Marks, 1993: The kinematic structure of Hurricane Gloria (1985) determined from nested analyses of dropwindsonde and Doppler radar data. *Mon. Wea. Rev.*, **121**, 2433–2451, [https://doi.org/10.1175/1520-0493\(1993\)121<2433:TKSOHG>2.0.CO;2](https://doi.org/10.1175/1520-0493(1993)121<2433:TKSOHG>2.0.CO;2).
- Galarneau, T. J., and C. A. Davis, 2013: Diagnosing forecast errors in tropical cyclone motion. *Mon. Wea. Rev.*, **141**, 405–430, <https://doi.org/10.1175/MWR-D-12-00071.1>.
- Gal-Chen, T., and R. C. Somerville, 1975: On the use of a coordinate transformation for the solution of the Navier-Stokes equations. *J. Comput. Phys.*, **17**, 209–228, [https://doi.org/10.1016/0021-9991\(75\)90037-6](https://doi.org/10.1016/0021-9991(75)90037-6).
- Gentry, R. C., 1983: Genesis of tornadoes associated with hurricanes. *Mon. Wea. Rev.*, **111**, 1793–1805, [https://doi.org/10.1175/1520-0493\(1983\)111<1793:GOTAWH>2.0.CO;2](https://doi.org/10.1175/1520-0493(1983)111<1793:GOTAWH>2.0.CO;2).
- Green, B. W., F. Zhang, and P. Markowski, 2011: Multiscale processes leading to supercells in the landfalling outer rainbands of Hurricane Katrina (2005). *Wea. Forecasting*, **26**, 828–847, <https://doi.org/10.1175/WAF-D-10-05049.1>.
- Gu, J.-F., Z.-M. Tan, and X. Qiu, 2018: The evolution of vortex tilt and vertical motion of tropical cyclones in directional shear flows. *J. Atmos. Sci.*, **75**, 3565–3578, <https://doi.org/10.1175/JAS-D-18-0024.1>.
- Hart, R., and J. Evans, 2001: A climatology of the extratropical transition of Atlantic tropical cyclones. *J. Climate*, **14**, 546–564, [https://doi.org/10.1175/1520-0442\(2001\)014<0546:ACOTET>2.0.CO;2](https://doi.org/10.1175/1520-0442(2001)014<0546:ACOTET>2.0.CO;2).
- Hawkins, H., and D. Rubsam, 1968: Hurricane Hilda, 1964. *Mon. Wea. Rev.*, **96**, 617–636, [https://doi.org/10.1175/1520-0493\(1968\)096<0617:HH>2.0.CO;2](https://doi.org/10.1175/1520-0493(1968)096<0617:HH>2.0.CO;2).
- Hence, D. A., and R. A. Houze, 2008: Kinematic structure of convective-scale elements in the rainbands of Hurricanes Katrina and Rita (2005). *J. Geophys. Res.*, **113**, D15108, <https://doi.org/10.1029/2007JD009429>.

- , and —, 2012: Vertical structure of tropical cyclone rainbands as seen by the TRMM precipitation radar. *J. Atmos. Sci.*, **69**, 2644–2661, <https://doi.org/10.1175/JAS-D-11-0323.1>.
- Hendricks, E. A., M. S. Peng, B. Fu, and T. Li, 2010: Quantifying environmental control on tropical cyclone intensity change. *Mon. Wea. Rev.*, **138**, 3243–3271, <https://doi.org/10.1175/2010MWR3185.1>.
- Hersbach, H., and Coauthors, 2020: The ERA5 global reanalysis. *Quart. J. Roy. Meteor. Soc.*, **146**, 1999–2049, <https://doi.org/10.1002/qj.3803>.
- Hock, T. F., and J. L. Franklin, 1999: The NCAR GPS dropwindsonde. *Bull. Amer. Meteor. Soc.*, **80**, 407–420, [https://doi.org/10.1175/1520-0477\(1999\)080<0407:TNGD>2.0.CO;2](https://doi.org/10.1175/1520-0477(1999)080<0407:TNGD>2.0.CO;2).
- Hodges, K., A. Cobb, and P. L. Vidale, 2017: How well are tropical cyclones represented in reanalysis datasets? *J. Climate*, **30**, 5243–5264, <https://doi.org/10.1175/JCLI-D-16-0557.1>.
- Houston, A. L., and R. B. Wilhelmson, 2007: Observational analysis of the 27 May 1997 central Texas tornadic event. Part I: Prestorm environment and storm maintenance/propagation. *Mon. Wea. Rev.*, **135**, 701–726, <https://doi.org/10.1175/MWR3300.1>.
- Hunter, J. D., 2007: Matplotlib: A 2D graphics environment. *Comput. Sci. Eng.*, **9**, 90–95, <https://doi.org/10.1109/MCSE.2007.55>.
- Jones, S. C., 1995: The evolution of vortices in vertical shear. I: Initially barotropic vortices. *Quart. J. Roy. Meteor. Soc.*, **121**, 821–851, <https://doi.org/10.1002/qj.49712152406>.
- , and Coauthors, 2003: The extratropical transition of tropical cyclones: Forecast challenges, current understanding, and future directions. *Wea. Forecasting*, **18**, 1052–1092, [https://doi.org/10.1175/1520-0434\(2003\)018<1052:TETOTC>2.0.CO;2](https://doi.org/10.1175/1520-0434(2003)018<1052:TETOTC>2.0.CO;2).
- Kaplan, J., and M. DeMaria, 1995: A simple empirical model for predicting the decay of tropical cyclone winds after landfall. *J. Appl. Meteor.*, **34**, 2499–2512, [https://doi.org/10.1175/1520-0450\(1995\)034<2499:ASEMFP>2.0.CO;2](https://doi.org/10.1175/1520-0450(1995)034<2499:ASEMFP>2.0.CO;2).
- , and —, 2003: Large-scale characteristics of rapidly intensifying tropical cyclones in the North Atlantic basin. *Wea. Forecasting*, **18**, 1093–1108, [https://doi.org/10.1175/1520-0434\(2003\)018<1093:LCORIT>2.0.CO;2](https://doi.org/10.1175/1520-0434(2003)018<1093:LCORIT>2.0.CO;2).
- , —, and J. A. Knaff, 2010: A revised tropical cyclone rapid intensification index for the Atlantic and eastern North Pacific basins. *Wea. Forecasting*, **25**, 220–241, <https://doi.org/10.1175/2009WAF2222280.1>.
- Kerns, B. W., and S. S. Chen, 2015: Subsidence warming as an underappreciated ingredient in tropical cyclogenesis. Part I: Aircraft observations. *J. Atmos. Sci.*, **72**, 4237–4260, <https://doi.org/10.1175/JAS-D-14-0366.1>.
- Klein, P., P. Harr, and R. Elsberry, 2000: Extratropical transition of western North Pacific tropical cyclones: An overview and conceptual model of the transformation stage. *Wea. Forecasting*, **15**, 373–395, [https://doi.org/10.1175/1520-0434\(2000\)015<0373:ETOWNP>2.0.CO;2](https://doi.org/10.1175/1520-0434(2000)015<0373:ETOWNP>2.0.CO;2).
- Knapp, K. R., M. C. Kruk, D. H. Levinson, H. J. Diamond, and C. J. Neumann, 2010: The International Best Track Archive for Climate Stewardship (IBTrACS): Unifying tropical cyclone data. *Bull. Amer. Meteor. Soc.*, **91**, 363–376, <https://doi.org/10.1175/2009BAMS2755.1>.
- Knapp, K. R., J. Walters, and M. Biggerstaff, 2006: Doppler profiler and radar observations of boundary layer variability during the landfall of Tropical Storm Gabrielle. *J. Atmos. Sci.*, **63**, 234–251, <https://doi.org/10.1175/JAS3608.1>.
- Markowski, P. M., and J. M. Straka, 2000: Some observations of rotating updrafts in a low-buoyancy, highly sheared environment. *Mon. Wea. Rev.*, **128**, 449–461, [https://doi.org/10.1175/1520-0493\(2000\)128<0449:SOORUI>2.0.CO;2](https://doi.org/10.1175/1520-0493(2000)128<0449:SOORUI>2.0.CO;2).
- , C. Hannon, J. Frame, E. Lancaster, A. Pietrycha, R. Edwards, and R. L. Thompson, 2003: Characteristics of vertical wind profiles near supercells obtained from the Rapid Update Cycle. *Wea. Forecasting*, **18**, 1262–1272, [https://doi.org/10.1175/1520-0434\(2003\)018<1262:COVWPN>2.0.CO;2](https://doi.org/10.1175/1520-0434(2003)018<1262:COVWPN>2.0.CO;2).
- Marks, F. D., R. A. Houze, and J. F. Gamache, 1992: Dual-aircraft investigation of the inner core of Hurricane Norbert. Part I: Kinematic structure. *J. Atmos. Sci.*, **49**, 919–942, [https://doi.org/10.1175/1520-0469\(1992\)049<0919:DAIOTI>2.0.CO;2](https://doi.org/10.1175/1520-0469(1992)049<0919:DAIOTI>2.0.CO;2).
- Martinaitis, S. M., 2017: Radar observations of tornado-warned convection associated with tropical cyclones over Florida. *Wea. Forecasting*, **32**, 165–186, <https://doi.org/10.1175/WAF-D-16-0105.1>.
- May, P. T., and G. J. Holland, 1999: The role of potential vorticity generation in tropical cyclone rainbands. *J. Atmos. Sci.*, **56**, 1224–1228, [https://doi.org/10.1175/1520-0469\(1999\)056<1224:TROPVG>2.0.CO;2](https://doi.org/10.1175/1520-0469(1999)056<1224:TROPVG>2.0.CO;2).
- May, R. M., S. C. Arms, P. Marsh, E. Bruning, J. R. Leeman, K. Goebbert, J. E. Thielen, and Z. S. Bruick, 2020: MetPy: A python package for meteorological data. Accessed 1 July 2018, <https://doi.org/10.5065/D6WW7G29>.
- McCaul, E. W., Jr., 1987: Observations of the hurricane “Danny” tornado outbreak of 16 August 1985. *Mon. Wea. Rev.*, **115**, 1206–1223, [https://doi.org/10.1175/1520-0493\(1987\)115<1206:OOTHTO>2.0.CO;2](https://doi.org/10.1175/1520-0493(1987)115<1206:OOTHTO>2.0.CO;2).
- , 1991: Buoyancy and shear characteristics of hurricane-tornado environments. *Mon. Wea. Rev.*, **119**, 1954–1978, [https://doi.org/10.1175/1520-0493\(1991\)119<1954:BASCOH>2.0.CO;2](https://doi.org/10.1175/1520-0493(1991)119<1954:BASCOH>2.0.CO;2).
- , and M. L. Weisman, 1996: Simulations of shallow supercell storms in landfalling hurricane environments. *Mon. Wea. Rev.*, **124**, 408–429, [https://doi.org/10.1175/1520-0493\(1996\)124<0408:SOSSSI>2.0.CO;2](https://doi.org/10.1175/1520-0493(1996)124<0408:SOSSSI>2.0.CO;2).
- , and —, 2001: The sensitivity of simulated supercell structure and intensity to variations in the shapes of environmental buoyancy and shear profiles. *Mon. Wea. Rev.*, **129**, 664–687, [https://doi.org/10.1175/1520-0493\(2001\)129<0664:TSOSSS>2.0.CO;2](https://doi.org/10.1175/1520-0493(2001)129<0664:TSOSSS>2.0.CO;2).
- Mercer, A. E., C. M. Shafer, C. A. Doswell III, L. M. Leslie, and M. B. Richman, 2012: Synoptic composites of tornadic and nontornadic outbreaks. *Mon. Wea. Rev.*, **140**, 2590–2608, <https://doi.org/10.1175/MWR-D-12-00029.1>.
- Merrill, R., 1984: A comparison of large and small tropical cyclones. *Mon. Wea. Rev.*, **112**, 1408–1418, [https://doi.org/10.1175/1520-0493\(1984\)112<1408:ACOLAS>2.0.CO;2](https://doi.org/10.1175/1520-0493(1984)112<1408:ACOLAS>2.0.CO;2).
- Molinari, J., and D. Vollaro, 2008: Extreme helicity and intense convective towers in Hurricane Bonnie. *Mon. Wea. Rev.*, **136**, 4355–4372, <https://doi.org/10.1175/2008MWR2423.1>.
- , and —, 2010: Distribution of helicity, CAPE, and shear in tropical cyclones. *J. Atmos. Sci.*, **67**, 274–284, <https://doi.org/10.1175/2009JAS3090.1>.
- , D. M. Romps, D. Vollaro, and L. Nguyen, 2012: CAPE in tropical cyclones. *J. Atmos. Sci.*, **69**, 2452–2463, <https://doi.org/10.1175/JAS-D-11-0254.1>.
- Murakami, H., 2014: Tropical cyclones in reanalysis data sets. *Geophys. Res. Lett.*, **41**, 2133–2141, <https://doi.org/10.1002/2014GL059519>.
- Nguyen, L. T., R. F. Rogers, and P. D. Reasor, 2017: Thermodynamic and kinematic influences on precipitation symmetry in sheared tropical cyclones: Bertha and Cristobal (2014). *Mon. Wea. Rev.*, **145**, 4423–4446, <https://doi.org/10.1175/MWR-D-17-0073.1>.
- , —, J. Zawislak, and J. A. Zhang, 2019: Assessing the influence of convective downdrafts and surface enthalpy fluxes on tropical cyclone intensity change in moderate vertical wind shear. *Mon. Wea. Rev.*, **147**, 3519–3534, <https://doi.org/10.1175/MWR-D-18-0461.1>.

- Nolan, D. S., 2011: Evaluating environmental favorableness for tropical cyclone development with the method of point-downscaling. *J. Adv. Model. Earth Syst.*, **3**, M08001, <https://doi.org/10.1029/2011MS000063>.
- Novlan, D. J., and W. M. Gray, 1974: Hurricane-spawned tornadoes. *Mon. Wea. Rev.*, **102**, 476–488, [https://doi.org/10.1175/1520-0493\(1974\)102<0476:HST>2.0.CO;2](https://doi.org/10.1175/1520-0493(1974)102<0476:HST>2.0.CO;2).
- Onderlinde, M. J., and D. S. Nolan, 2014: Environmental helicity and its effects on development and intensification of tropical cyclones. *J. Atmos. Sci.*, **71**, 4308–4320, <https://doi.org/10.1175/JAS-D-14-0085.1>.
- , and —, 2016: Tropical cyclone–relative environmental helicity and the pathways to intensification in shear. *J. Atmos. Sci.*, **73**, 869–890, <https://doi.org/10.1175/JAS-D-15-0261.1>.
- Parker, M. D., 2014: Composite VORTEX2 supercell environments from near-storm soundings. *Mon. Wea. Rev.*, **142**, 508–529, <https://doi.org/10.1175/MWR-D-13-00167.1>.
- Paterson, L. A., B. N. Hanstrum, N. E. Davidson, and H. C. Weber, 2005: Influence of environmental vertical wind shear on the intensity of hurricane-strength tropical cyclones in the Australian region. *Mon. Wea. Rev.*, **133**, 3644–3660, <https://doi.org/10.1175/MWR3041.1>.
- Pearson, A., and A. Sadowski, 1965: Hurricane-induced tornadoes and their distribution. *Mon. Wea. Rev.*, **93**, 461–464, [https://doi.org/10.1175/1520-0493\(1965\)093<0461:HITATD>2.3.CO;2](https://doi.org/10.1175/1520-0493(1965)093<0461:HITATD>2.3.CO;2).
- Potvin, C. K., K. L. Elmore, and S. J. Weiss, 2010: Assessing the impacts of proximity sounding criteria on the climatology of significant tornado environments. *Wea. Forecasting*, **25**, 921–930, <https://doi.org/10.1175/2010WAF222368.1>.
- Powell, M., P. Vickery, and T. Reinhold, 2003: Reduced drag coefficient for high wind speeds in tropical cyclones. *Nature*, **422**, 279–283, <https://doi.org/10.1038/nature01481>.
- Ramsay, H. A., and C. A. Doswell III, 2005: A sensitivity study of hodograph-based methods for estimating supercell motion. *Wea. Forecasting*, **20**, 954–970, <https://doi.org/10.1175/WAF889.1>.
- Rasmussen, E. N., 2003: Refined supercell and tornado forecast parameters. *Wea. Forecasting*, **18**, 530–535, [https://doi.org/10.1175/1520-0434\(2003\)18<530:RSATFP>2.0.CO;2](https://doi.org/10.1175/1520-0434(2003)18<530:RSATFP>2.0.CO;2).
- , and D. O. Blanchard, 1998: A baseline climatology of sounding-derived supercell and tornado forecast parameters. *Wea. Forecasting*, **13**, 1148–1164, [https://doi.org/10.1175/1520-0434\(1998\)013<1148:ABCOSD>2.0.CO;2](https://doi.org/10.1175/1520-0434(1998)013<1148:ABCOSD>2.0.CO;2).
- , and J. M. Straka, 1998: Variations in supercell morphology. Part I: Observations of the role of upper-level storm-relative flow. *Mon. Wea. Rev.*, **126**, 2406–2421, [https://doi.org/10.1175/1520-0493\(1998\)126<2406:VISMPI>2.0.CO;2](https://doi.org/10.1175/1520-0493(1998)126<2406:VISMPI>2.0.CO;2).
- Raymond, D., 1992: Nonlinear balance and potential-vorticity thinking at large Rossby number. *Quart. J. Roy. Meteor. Soc.*, **118**, 987–1015, <https://doi.org/10.1002/qj.49711850708>.
- Reasor, P. D., and M. T. Montgomery, 2015: Evaluation of a heuristic model for tropical cyclone resilience. *J. Atmos. Sci.*, **72**, 1765–1782, <https://doi.org/10.1175/JAS-D-14-0318.1>.
- , —, and L. Grasso, 2004: A new look at the problem of tropical cyclones in vertical shear flow: Vortex resiliency. *J. Atmos. Sci.*, **61**, 3–22, [https://doi.org/10.1175/1520-0469\(2004\)061<0003:ANLATP>2.0.CO;2](https://doi.org/10.1175/1520-0469(2004)061<0003:ANLATP>2.0.CO;2).
- , R. Rogers, and S. Lorsolo, 2013: Environmental flow impacts on tropical cyclone structure diagnosed from airborne Doppler radar composites. *Mon. Wea. Rev.*, **141**, 2949–2969, <https://doi.org/10.1175/MWR-D-12-00334.1>.
- Riemer, M., M. T. Montgomery, and M. E. Nicholls, 2010: A new paradigm for intensity modification of tropical cyclones: Thermodynamic impact of vertical wind shear on the inflow layer. *Atmos. Chem. Phys.*, **10**, 3163–3188, <https://doi.org/10.5194/acp-10-3163-2010>.
- Rios-Berrios, R., and R. D. Torn, 2017: Climatological analysis of tropical cyclone intensity changes under moderate vertical wind shear. *Mon. Wea. Rev.*, **145**, 1717–1738, <https://doi.org/10.1175/MWR-D-16-0350.1>.
- , —, and C. A. Davis, 2016a: An ensemble approach to investigate tropical cyclone intensification in sheared environments. Part I: Katia (2011). *J. Atmos. Sci.*, **73**, 71–93, <https://doi.org/10.1175/JAS-D-15-0052.1>.
- , —, and —, 2016b: An ensemble approach to investigate tropical cyclone intensification in sheared environments. Part II: Ophelia (2011). *J. Atmos. Sci.*, **73**, 1555–1575, <https://doi.org/10.1175/JAS-D-15-0245.1>.
- Ritchie, E. A., and R. L. Elsberry, 2001: Simulations of the transformation stage of the extratropical transition of tropical cyclones. *Mon. Wea. Rev.*, **129**, 1462–1480, [https://doi.org/10.1175/1520-0493\(2001\)129<1462:SOTTO>2.0.CO;2](https://doi.org/10.1175/1520-0493(2001)129<1462:SOTTO>2.0.CO;2).
- Rogers, R. F., J. A. Zhang, J. Zawislak, H. Jiang, G. R. Alvey III, E. J. Zipser, and S. N. Stevenson, 2016: Observations of the structure and evolution of Hurricane Edouard (2014) during intensity change. Part II: Kinematic structure and the distribution of deep convection. *Mon. Wea. Rev.*, **144**, 3355–3376, <https://doi.org/10.1175/MWR-D-16-0017.1>.
- Romps, D. M., and Z. Kuang, 2011: A transilient matrix for moist convection. *J. Atmos. Sci.*, **68**, 2009–2025, <https://doi.org/10.1175/2011JAS3712.1>.
- Ryglicki, D. R., J. H. Cossuth, D. Hodyss, and J. D. Doyle, 2018: The unexpected rapid intensification of tropical cyclones in moderate vertical wind shear. Part I: Overview and observations. *Mon. Wea. Rev.*, **146**, 3773–3800, <https://doi.org/10.1175/MWR-D-18-0020.1>.
- Schenkel, B., and R. Hart, 2012: An examination of tropical cyclone position, intensity, and intensity life cycle within atmospheric reanalysis datasets. *J. Climate*, **25**, 3453–3475, <https://doi.org/10.1175/2011JCLI4208.1>.
- , N. Lin, D. Chavas, M. Oppenheimer, and A. Brammer, 2017: Evaluating outer tropical cyclone size in reanalysis datasets using QuikSCAT data. *J. Climate*, **30**, 8745–8762, <https://doi.org/10.1175/JCLI-D-17-0122.1>.
- , —, —, G. Vecchi, M. Oppenheimer, and A. Brammer, 2018: The lifetime evolution of outer tropical cyclone size. *J. Climate*, **31**, 7985–8004, <https://doi.org/10.1175/JCLI-D-17-0630.1>.
- Schultz, L. A., and D. J. Cecil, 2009: Tropical cyclone tornadoes, 1950–2007. *Mon. Wea. Rev.*, **137**, 3471–3484, <https://doi.org/10.1175/2009MWR2896.1>.
- Shafer, C. M., A. E. Mercer, L. M. Leslie, M. B. Richman, and C. A. Doswell III, 2010: Evaluation of WRF Model simulations of tornadic and nontornadic outbreaks occurring in the spring and fall. *Mon. Wea. Rev.*, **138**, 4098–4119, <https://doi.org/10.1175/2010MWR3269.1>.
- Shapiro, L. J., 1983: The asymmetric boundary layer flow under a translating hurricane. *J. Atmos. Sci.*, **40**, 1984–1998, [https://doi.org/10.1175/1520-0469\(1983\)040<1984:TABLFU>2.0.CO;2](https://doi.org/10.1175/1520-0469(1983)040<1984:TABLFU>2.0.CO;2).
- Simpson, R., and H. Riehl, 1958: Midtropospheric ventilation as a constraint on hurricane development and maintenance. *Tech. Conf. on Hurricanes*, Miami Beach, FL, Amer. Meteor. Soc., D4-1–D4-10.
- Spratt, S. M., D. W. Sharp, P. Welsh, A. Sandrik, F. Alsheimer, and C. Paxton, 1997: A WSR-88D assessment of tropical cyclone outer rainband tornadoes. *Wea. Forecasting*, **12**, 479–501, [https://doi.org/10.1175/1520-0434\(1997\)012<0479:AWAOTC>2.0.CO;2](https://doi.org/10.1175/1520-0434(1997)012<0479:AWAOTC>2.0.CO;2).

- Stevenson, S. N., K. L. Corbosiero, and S. F. Abarca, 2016: Lightning in eastern North Pacific tropical cyclones: A comparison to the North Atlantic. *Mon. Wea. Rev.*, **144**, 225–239, <https://doi.org/10.1175/MWR-D-15-0276.1>.
- , —, M. DeMaria, and J. L. Vigh, 2018: A 10-year survey of tropical cyclone inner-core lightning bursts and their relationship to intensity change. *Wea. Forecasting*, **33**, 23–36, <https://doi.org/10.1175/WAF-D-17-0096.1>.
- Stewart, S., and R. Berg, 2019: Tropical cyclone report: Hurricane Florence (31 August–17 September 2018). NHC Tech. Rep. AL062018, 98 pp., https://www.nhc.noaa.gov/data/tcr/AL062018_Florence.pdf.
- Suzuki, O., H. Niino, H. Ohno, and H. Nirasawa, 2000: Tornado-producing mini supercells associated with Typhoon 9019. *Mon. Wea. Rev.*, **128**, 1868–1882, [https://doi.org/10.1175/1520-0493\(2000\)128<1868:TPMSAW>2.0.CO;2](https://doi.org/10.1175/1520-0493(2000)128<1868:TPMSAW>2.0.CO;2).
- Tang, B., and K. Emanuel, 2010: Midlevel ventilation's constraint on tropical cyclone intensity. *J. Atmos. Sci.*, **67**, 1817–1830, <https://doi.org/10.1175/2010JAS3318.1>.
- , and —, 2012: A ventilation index for tropical cyclones. *Bull. Amer. Meteor. Soc.*, **93**, 1901–1912, <https://doi.org/10.1175/BAMS-D-11-00165.1>.
- , and S. J. Camargo, 2014: Environmental control of tropical cyclones in CMIP5: A ventilation perspective. *J. Adv. Model. Earth Syst.*, **6**, 115–128, <https://doi.org/10.1002/2013MS000294>.
- Thompson, R. L., R. Edwards, J. A. Hart, K. L. Elmore, and P. Markowski, 2003: Close proximity soundings within supercell environments obtained from the Rapid Update Cycle. *Wea. Forecasting*, **18**, 1243–1261, [https://doi.org/10.1175/1520-0434\(2003\)018<1243:CPSWSE>2.0.CO;2](https://doi.org/10.1175/1520-0434(2003)018<1243:CPSWSE>2.0.CO;2).
- Ueno, M., 2007: Observational analysis and numerical evaluation of the effects of vertical wind shear on the rainfall asymmetry in the typhoon inner-core region. *J. Meteor. Soc. Japan*, **85**, 115–136, <https://doi.org/10.2151/jmsj.85.115>.
- Verbout, S. M., D. M. Schultz, L. M. Leslie, H. E. Brooks, D. Karoly, and K. L. Elmore, 2007: Tornado outbreaks associated with landfalling hurricanes in the North Atlantic basin: 1954–2004. *Meteor. Atmos. Phys.*, **97**, 255–271, <https://doi.org/10.1007/s00703-006-0256-x>.
- Warren, R. A., H. Richter, H. A. Ramsay, S. T. Siems, and M. J. Manton, 2017: Impact of variations in upper-level shear on simulated supercells. *Mon. Wea. Rev.*, **145**, 2659–2681, <https://doi.org/10.1175/MWR-D-16-0412.1>.
- Wingo, M. T., and D. J. Cecil, 2010: Effects of vertical wind shear on tropical cyclone precipitation. *Mon. Wea. Rev.*, **138**, 645–662, <https://doi.org/10.1175/2009MWR2921.1>.
- Wu, W.-S., D. K. Lilly, and R. M. Kerr, 1992: Helicity and thermal convection with shear. *J. Atmos. Sci.*, **49**, 1800–1809, [https://doi.org/10.1175/1520-0469\(1992\)049<1800:HATCWS>2.0.CO;2](https://doi.org/10.1175/1520-0469(1992)049<1800:HATCWS>2.0.CO;2).
- Yamei, X., and W. Rongsheng, 2003: The conservation of helicity in Hurricane Andrew (1992) and the formation of the spiral rainband. *Adv. Atmos. Sci.*, **20**, 940–950, <https://doi.org/10.1007/BF02915517>.
- Zawislak, J., H. Jiang, G. R. Alvey III, E. J. Zipser, R. F. Rogers, J. A. Zhang, and S. N. Stevenson, 2016: Observations of the structure and evolution of Hurricane Edouard (2014) during intensity change. Part I: Relationship between the thermodynamic structure and precipitation. *Mon. Wea. Rev.*, **144**, 3333–3354, <https://doi.org/10.1175/MWR-D-16-0018.1>.
- Zhang, J. A., R. F. Rogers, P. D. Reasor, E. W. Uhlhorn, and F. D. Marks, 2013: Asymmetric hurricane boundary layer structure from dropsonde composites in relation to the environmental vertical wind shear. *Mon. Wea. Rev.*, **141**, 3968–3984, <https://doi.org/10.1175/MWR-D-12-00335.1>.

Corrigendum

BENJAMIN A. SCHENKEL,^{a,b,c} ROGER EDWARDS,^d AND MICHAEL CONIGLIO^c

^a *Cooperative Institute for Mesoscale Meteorological Studies, University of Oklahoma,
Norman, Oklahoma*

^b *School of Meteorology, University of Oklahoma, Norman, Oklahoma*

^c *NOAA/NSSL, Norman, Oklahoma*

^d *NOAA/SPC, Norman, Oklahoma*

(Manuscript received 13 April 2021, in final form 30 April 2021)

An error was discovered in the inadvertent inclusion of tropical cyclone (TC) motion from both the composite hodographs (Fig. 12) and vertical profiles of TC-relative tangential and radial winds (Fig. 13) computed from radiosondes sampling landfalling TCs in Schenkel et al. (2020). There are two primary reasons why TC motion should have been removed from these figures. First, the inclusion of TC motion makes it impossible to determine whether changes in the total wind field are due to the ambient or TC wind field when Fig. 12 and especially Fig. 13 were focused on differences in the latter. Second, exclusion of TC motion is consistent with previous studies of TC tornadoes (McCaul 1991; Baker et al. 2009) and the response of the TC circulation to ambient deep-tropospheric vertical wind shear (VWS; Zhang et al. 2013; DeHart et al. 2014). The removal of TC motion shows that only the TC secondary circulation strengthens with increasing VWS, which contrasts with Schenkel et al. (2020) that incorrectly showed increases in both the TC primary and secondary circulation. More specific details on these changes to the conclusions and the revised versions of Figs. 12 and 13 are discussed below.

The removal of TC motion from the composite hodographs in Fig. 12 shows a shift in the hodographs with no changes to the overarching conclusions. However, these revisions to Fig. 12 enable more direct comparison with hodographs shown in prior studies of TC tornadoes where TC motion is removed (McCaul 1991; Baker et al. 2009).

In contrast to Fig. 12, the revised version of Fig. 13 shows that the TC secondary circulation, and not the primary circulation, statistically strengthens in the downshear quadrants and weakens in the upshear quadrants with increasing VWS. These results are consistent with previous work (Black et al. 2002; Molinari and Vollaro 2010). Focusing on the downshear-left and downshear-right quadrants, the radial wind speed more than doubles between the weak and strong VWS categories. Moreover, the largest magnitude changes occur between 250 and 500 m above the surface, especially in the downshear-right quadrant. It is this strengthening of the TC secondary circulation and the associated stronger convective-scale vertical wind shear that likely partially supports favorable kinematic environments for tornadoes as suggested by prior work (Molinari and Vollaro 2008, 2010). In the original manuscript, the constructive superposition between increasing north-northeastward TC motion associated with stronger VWS and the TC winds in the downshear-right quadrant (Corbosiero and Molinari 2003; Schenkel et al. 2020) provided the false impression that the primary circulation was strengthening in this quadrant. Instead, except for the upshear-left quadrant, the exclusion of TC motion in Fig. 13 shows no statistical changes in the TC primary circulation in any quadrant with increasing VWS.

Together, these changes do not alter the primary conclusions of the manuscript that VWS impacts both the frequency and location of TC tornadoes. Rather, this corrigendum shows changes in one potential physical explanation for how strong VWS provides favorable kinematic environments for TC tornadoes. Namely, only the secondary circulation (and not the primary circulation) strengthens with stronger VWS with increases that are beyond those shown in Schenkel et al. (2020). This larger enhancement of only the TC secondary circulation, and associated strengthening of convective-scale vertical wind shear, likely partially explains why kinematic environments in the downshear sectors more strongly support tornadoes as VWS increases.

Corresponding author: Benjamin A. Schenkel, benschenkel@gmail.com

DOI: 10.1175/WAF-D-21-0055.1

© 2021 American Meteorological Society. For information regarding reuse of this content and general copyright information, consult the [AMS Copyright Policy](#) ([www.ametsoc.org/PUBSReuseLicenses](#)).

Brought to you by NOAA Central Library | Unauthenticated | Downloaded 09/02/21 08:53 PM UTC

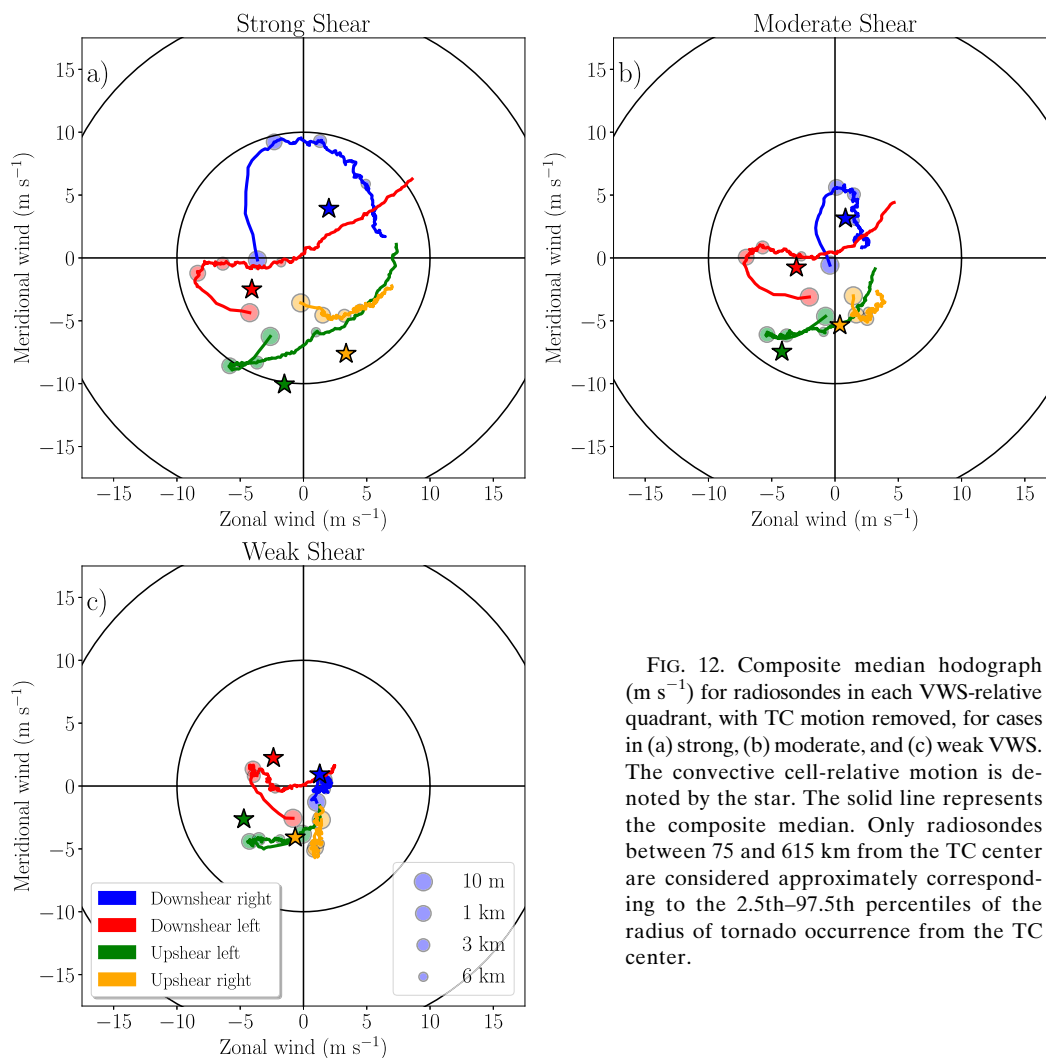


FIG. 12. Composite median hodograph (m s^{-1}) for radiosondes in each VWS-relative quadrant, with TC motion removed, for cases in (a) strong, (b) moderate, and (c) weak VWS. The convective cell-relative motion is denoted by the star. The solid line represents the composite median. Only radiosondes between 75 and 615 km from the TC center are considered approximately corresponding to the 2.5th–97.5th percentiles of the radius of tornado occurrence from the TC center.

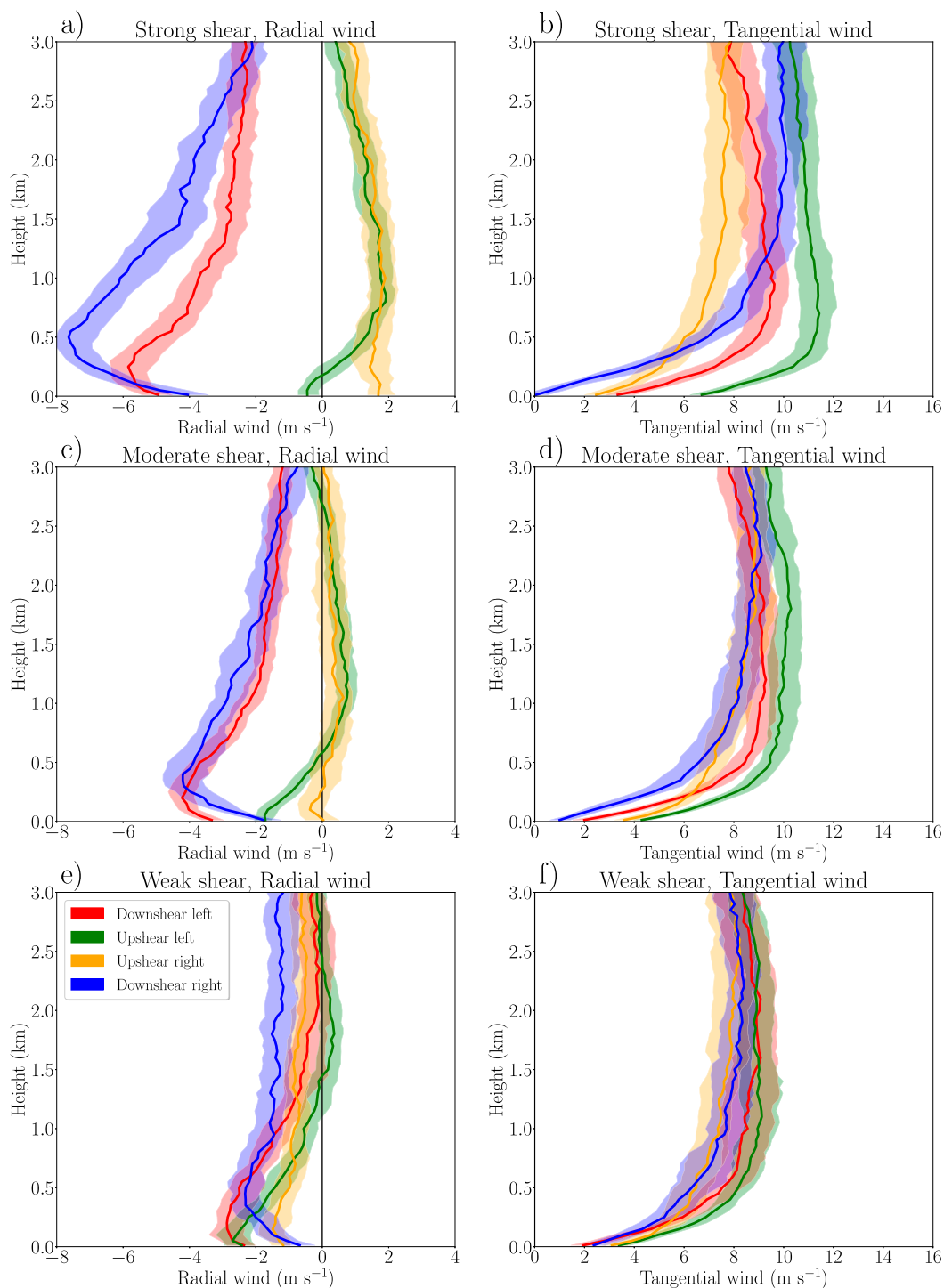


FIG. 13. Composite median (solid line) and its 95% confidence interval (shading) of vertical profiles of cyclone-relative radial wind (m s^{-1}) and tangential wind (m s^{-1}), with TC motion removed, computed from radiosondes in each of the VWS-relative quadrants for TCs in (a),(b) strong; (c),(d) moderate; and (e),(f) weak VWS. Only radiosondes between 75 and 615 km from the TC center are considered approximately corresponding to the 2.5th–97.5th percentiles of the radius of tornado occurrence from the TC center.

REFERENCES

- Baker, A. K., M. D. Parker, and M. D. Eastin, 2009: Environmental ingredients for supercells and tornadoes within Hurricane Ivan. *Wea. Forecasting*, **24**, 223–244, <https://doi.org/10.1175/2008WAF2222146.1>.
- Black, M., J. Gamache, F. Marks, C. Samsury, and H. Willoughby, 2002: Eastern Pacific Hurricanes Jimena of 1991 and Olivia of 1994: The effect of vertical shear on structure and intensity. *Mon. Wea. Rev.*, **130**, 2291–2312, [https://doi.org/10.1175/1520-0493\(2002\)130<2291:EPHJOA>2.0.CO;2](https://doi.org/10.1175/1520-0493(2002)130<2291:EPHJOA>2.0.CO;2).
- Corbosiero, K., and J. Molinari, 2003: The relationship between storm motion, vertical wind shear, and convective asymmetries in tropical cyclones. *J. Atmos. Sci.*, **60**, 366–376, [https://doi.org/10.1175/1520-0469\(2003\)060<0366:TRBSMV>2.0.CO;2](https://doi.org/10.1175/1520-0469(2003)060<0366:TRBSMV>2.0.CO;2).
- DeHart, J. C., R. A. Houze, and R. F. Rogers, 2014: Quadrant distribution of tropical cyclone inner-core kinematics in relation to environmental shear. *J. Atmos. Sci.*, **71**, 2713–2732, <https://doi.org/10.1175/JAS-D-13-0298.1>.
- McCaul, E. W., 1991: Buoyancy and shear characteristics of hurricane–tornado environments. *Mon. Wea. Rev.*, **119**, 1954–1978, [https://doi.org/10.1175/1520-0493\(1991\)119<1954:BASCOH>2.0.CO;2](https://doi.org/10.1175/1520-0493(1991)119<1954:BASCOH>2.0.CO;2).
- Molinari, J., and D. Vollaro, 2008: Extreme helicity and intense convective towers in Hurricane Bonnie. *Mon. Wea. Rev.*, **136**, 4355–4372, <https://doi.org/10.1175/2008MWR2423.1>.
- , and —, 2010: Distribution of helicity, CAPE, and shear in tropical cyclones. *J. Atmos. Sci.*, **67**, 274–284, <https://doi.org/10.1175/2009JAS3090.1>.
- Schenkel, B., R. Edwards, and M. Coniglio, 2020: A climatological analysis of ambient deep-tropospheric vertical wind shear impacts upon tornadic supercells in tropical cyclones. *Wea. Forecasting*, **35**, 2033–2059, <https://doi.org/10.1175/WAF-D-19-0220.1>.
- Zhang, J. A., R. F. Rogers, P. D. Reasor, E. W. Uhlhorn, and F. D. Marks, 2013: Asymmetric hurricane boundary layer structure from dropsonde composites in relation to the environmental vertical wind shear. *Mon. Wea. Rev.*, **141**, 3968–3984, <https://doi.org/10.1175/MWR-D-12-00335.1>.